Available online at www.sciencedirect.com

ScienceDirect

Geochimica et Cosmochimica Acta 75 (2011) 4728–4751

Geochimica et Cosmochimica Acta

www.elsevier.com/locate/gca

CO_2–water–basalt interaction. Numerical simulation of low temperature CO_2 sequestration into basalts

Alexander P. Gysi *, Andri Stefánsson

Institute of Earth Sciences, University of Iceland, Sturlugata 7, 101 Reykjavik, Iceland

Received 13 January 2011; accepted in revised form 29 April 2011; available online 11 July 2011

Abstract

The interaction between CO_2-rich waters and basaltic glass was studied using reaction path modeling in order to get insight into the water–rock reaction process including secondary mineral composition, water chemistry and mass transfer as a function of CO_2 concentration and reaction progress (ξ). The calculations were carried out at 25–90 °C and pCO_2 to 30 bars and the results were compared to recent experimental observations and natural systems. A thermodynamic dataset was compiled from 25 to 300 °C in order to simulate mineral saturations relevant to basalt alteration in CO_2-rich environment including revised key aqueous species for mineral dissolution reactions and apparent Gibbs energies for clay and carbonate solid solutions observed to form in nature. The dissolution of basaltic glass in CO_2-rich waters was found to be incongruent with the overall water composition and secondary mineral formation depending on reaction progress and pH. Under mildly acid conditions in CO_2 enriched waters (pH <6.5), SiO_2 and simple Al–Si minerals, Ca–Mg–Fe smectites and Ca–Mg–Fe carbonates predominated. Iron, Al and Si were immobile whereas the Mg and Ca mobility depended on the mass of carbonate formed and water pH. Upon quantitative CO_2 mineralization, the pH increased to >8 resulting in Ca–Mg–Fe smectite, zeolites and calcite formation, reducing the mobility of most dissolved elements. The dominant factor determining the reaction path of basalt alteration and the associated element mobility was the pH of the water. In turn, the pH value was determined by the concentration of CO_2 and extent of reaction. The composition of the carbonates depended on the mobility of Ca, Mg and Fe. At pH <6.5, Fe was in the ferrous oxidation state resulting in the formation of Fe-rich carbonates with the incorporation of Ca and Mg. At pH >8, the mobility of Fe and Mg was limited due to the formation of clays whereas Ca was incorporated into calcite, zeolites and clays. Competing reactions between clays (Ca–Fe smectites) and carbonates at low pH, and zeolites and clays (Mg–Fe smectites) and carbonates at high pH, controlled the availability of Ca, Mg and Fe, playing a key role for low temperature CO_2 mineralization and sequestration into basalts. Several problems of the present model point to the need of improvement in future work. The determinant factors linking time to low temperature reaction path modeling may not only be controlled by the primary dissolving phase, which presents challenges concerning non-stoichiometric dissolution, the leached layer model and reactive surface area, but may include secondary mineral precipitation kinetics as rate limiting step for specific reactions such as retrieved from the present reaction path study.

1. INTRODUCTION

Carbon dioxide is among the most common acids in natural systems and plays a fundamental role in geochemical reactions and cycles at and near the Earth's surface (e.g. Berner and Berner, 1995; Gíslason et al., 1996; Gaillardet et al., 1999; Dessert et al., 2003). Increased anthropogenic CO_2 emissions have caused an imbalance in the CO_2 cycle and resulted in climate change (Allen et al., 2009). Sequestration by mineral carbonation is considered a possible option of trapping the CO_2 on geological time scales (e.g. Xu et al., 2004; Goldberg et al., 2008; Kelemen and Matter, 2008; Oelkers et al., 2008). Mafic and ultramafic rocks

---

* Corresponding author. Tel.: +354 5255248.
E-mail address: apg2@hi.is (A.P. Gysi).

0016-7037/$ - see front matter © 2011 Elsevier Ltd. All rights reserved.
doi:10.1016/j.gca.2011.05.037

provide good candidates for such carbonate sequestration due to high availability of divalent cations like Mg^{2+}, Ca^{2+} and Fe^{2+} (McGrail et al., 2006; Goldberg et al., 2008; Kelemen and Matter, 2008; Garcia et al., 2010; Schaef et al., 2010) and field-scale studies have been launched in order to assess whether low temperature CO_2 sequestration is feasible (e.g. Matter et al., 2009; Gíslason et al., 2010). One of the problems associated with CO_2 sequestration into basalts are the detailed effects of rock composition and crystallinity, acid supply and extent of reaction or time on the secondary mineralogy, water composition and mass fluxes. Such understanding is critical for long-term assessment of the feasibility of carbonate mineralization in basaltic rock formations.

The alteration of basalts and basaltic glasses has been the subject of number of studies. Detailed observation of low temperature alteration products and the related changes in water chemistry has resulted in considerable gain in understanding of the basalt–water interaction process (e.g. Furnes, 1975; Eggleton and Keller, 1982; Gíslason and Eugster, 1987a,b; Thorseth et al., 1991; Crovisier et al., 1992; Ghiara et al., 1993; Gíslason et al., 1993; Daux et al., 1994, 1997; Ghiara and Petti, 1996; Neuhoff et al., 1999; Stefánsson and Gíslason, 2001; Stroncik and Schmincke, 2001). At low-temperatures, the alteration and weathering of basaltic glasses results in the formation of an amorphous gel on the surface generally termed “palagonite” (Stroncik and Schmincke, 2001). These fine alteration layers are similar to alteration films associated with borosilicate glasses used for nuclear waste disposal (Crovisier et al., 2003). With time, the alteration layer formed on the glass surface becomes a heterogeneous substance composed of variable phases including clays, zeolites, oxides and hydroxides with smectites usually predominating (Eggleton and Keller, 1982; Furnes, 1984; Jercinovic et al., 1990; Zhou et al., 1992; Stroncik and Schmincke, 2001). Titanium, Fe and Al are considered to be fully retained in the secondary minerals during alteration and to lesser extend Si, whereas Na, K, Ca and Mg show variable mobility partly depending on the reaction progress (Staudigel and Hart, 1983; Crovisier et al., 1992; Daux et al., 1994; Gíslason et al., 1996; Stefánsson and Gíslason, 2001; Stroncik and Schmincke, 2001).

Reaction path simulations have provided important insights into the basalt alteration process when combined with natural system and experimental observations (Gíslason and Eugster, 1987a; Crovisier et al., 1992; Gíslason et al., 1993; Stefánsson and Gíslason, 2001). The secondary mineralogy associated with low temperature basalt alteration consists primarily of amorphous aluminum hydroxide and ferrihydrite, Mg–Fe smectites and Al–Si minerals (allophane and/or imogolite) whereas at higher reaction progress when more basalt has reacted the mineralogy consists of Ca–Na zeolites, Fe–Mg rich clays and calcite (e.g. Gíslason et al., 1993; Neuhoff et al., 1999; Stefánsson and Gíslason, 2001). Observations based on elevated CO_2–basalt alteration from the Disko-Nuussuaq Island (West Greenland) are somewhat different and indicate quartz, Fe–Mg carbonates and Ca–Mg carbonates to be among the dominant secondary mineral assemblages (Rogers et al., 2006). Preliminary reaction path calculations have shown that these minerals are probably thermodynamically stable and that the reaction path of water–basalt interaction is considerably changed when CO_2 is added to the system (Gysi and Stefánsson, 2008). However, the overall CO_2–water–basalt interaction process is geochemically complex and the key processes affecting the chemical mass fluxes between primary dissolving minerals, CO_2 enriched waters and secondary mineral precipitation reactions remain unclear.

Our approach in understanding these processes consisted of combining and comparing reaction path simulations with laboratory experiments and observations from natural systems in order to develop a conceptual model of the overall CO_2–water–basalt reaction process. The studied model includes the integrated effects of CO_2 concentration on secondary mineral composition, water chemistry and mass fluxes between primary and secondary minerals and the solution from 25 to 90 °C and initial $p\mathrm{CO}_2$ of <1–30 bar.

2. MODEL CALCULATIONS

2.1. Reaction path modeling

Reaction path modeling (e.g. Helgeson, 1968; Denbigh, 1971; Marini, 2006) was carried out between CO_2-rich waters and basalt using the PHREEQC geochemical program (Parkhurst and Appelo, 1999). The geochemical reactions were studied as a function of reaction progress (ξ) including basalt dissolution, secondary mineral formation and water chemistry. The reaction progress can be linked to either the moles of reacted primary phase or reaction time given that the rates of reactions are known as well as the mineral reactive surface areas. In the present study, the water was allowed to react with basaltic glass in accordance with the dissolution rates reported by Gíslason and Oelkers (2003) and the saturated secondary minerals were allowed to precipitate in each simulated step assuming instantaneous equilibration. The time was linked to reaction progress (ξ-time) throughout this study in order to indicate that the factor time has limited meaning in reaction path studies, but effectively reflects the progress of reaction during irreversible reactions.

In the calculations, the basalt was taken to be a homogeneous basaltic glass similar to the glass from Stapafell (Southwest Iceland) used in our previous experiments (Gysi and Stefánsson, 2011). Its composition and physical properties are listed in Table 1. The initial water composition used in the simulations are listed in Table 2 and consisted of natural spring water from Vellankatla, Southwest Iceland, and precipitation from the Langjökull ice cap, Central Iceland. Two sets of reaction path calculations were carried out in order to simulate atmospheric and elevated CO_2 systems, respectively. The simulated conditions are summarized in Table 3. In the first set, 10 g of Stapafell glass was allowed to dissolve in 1 kg water both opened and closed to atmospheric CO_2 in order to model natural basalt weathering. In the second set, 100–200 g basaltic glass was allowed to dissolve in 1 kg water at initial $p\mathrm{CO}_2$ of 1–30 bar

Table 1
Physical and chemical properties of the Stapafell basaltic glass (BG) and kinetic parameters.

BG dissolution reaction	$K_{0.008}Na_{0.08}Ca_{0.27}Mg_{0.26}Mn_{0.003}Ti_{0.02}Fe^{2+}_{0.169}Fe^{3+}_{0.012}Al_{0.35}Si_{1.00}O_{3.329} + 1.13H^+ + 2.199H_2O = 0.008\ K^+ + 0.08Na^+ + 0.27Ca^{2+} + 0.26\ Mg^{2+} + 0.003Mn^{2+} + 0.02Ti(OH)_4 + 0.169Fe^{2+} + 0.012Fe(OH)_4^- + 0.35Al(OH)_4^- + H_4SiO_4^0$
Leached layer formula	$SiAl_{0.35}O_2(OH)_{1.05}$
Molecular wt. BG	121.3 g/mol
Grain diameter (d)	$d_{min-max} = 45$–125 μm
Geometric surface area	250 cm^2/g

Table 2
Initial solution composition used in the simulations. Units are in μmol/kg.

	Vellankatla spring	Langjökull precipitation[a]
pH/°C	7.84/25	5.73/25
CO_2	354	13.35
Si	256	0.001
Na	269	3.1
K	11.9	0.45
Ca	71	0.15
Mg	38	0.35
Fe	0.16	0.013
Al	1.09	0.054
SO_4	15	0.35
Cl	120	3.15

[a] Pogge von Strandmann et al. (2008).

Table 3
Initial parameters used for the reaction path simulations.

Parameters	Atmospheric CO_2	Elevated CO_2
pCO_2 (bar)	3.2×10^{-4}	1–30
t (°C)	25	25–90
pe	Fe(+II)/Fe(+III) (closed); O(−II)/O(0) (open)	Fe(+II)/Fe(+III) (closed)
Rock/water (g/l)	10	100–200
Initial water	Langjökull, Vellankatla	Vellankatla

to model the effects of CO_2 on the water–basalt reaction path. The calculations were conducted at 25, 40 and 90 °C to study the effects of temperature.

The redox state of the solutions was modeled in two ways. Firstly, it was taken to reflect the supply of Fe(II) and Fe(III) from the dissolution of the basaltic glass and consumption of Fe by secondary minerals (more reduced Fe in a closed system), and secondly, assuming atmospheric oxygen saturation (more oxidized Fe in an open system). The pe value was calculated using the Fe(II) to Fe(III) ratios or the O(−II) to O(0) ratios in solution, respectively. Secondary mineral precipitation–dissolution reactions were assumed to be controlled by their saturation state in solution defined as the log of the ratio Q/K represented by the reaction quotient (Q) and the equilibrium constant (K) of the mineral dissolution reaction. Secondary minerals allowed to precipitate during the simulations were selected based on the secondary mineralogy observed during low temperature basalt weathering and CO_2–water–basalt interaction in nature and experiments (Gíslason and Eugster, 1987a,b; Crovisier et al., 1992; Ghiara et al., 1993; Gíslason et al., 1993, 1996; Ghiara and Petti, 1996; Daux et al., 1997; Neuhoff et al., 1999; Stefánsson and Gíslason, 2001; Rogers et al., 2006). The compositions of the secondary minerals considered and their dissolution reactions are listed in Table 4.

2.2. Basaltic glass dissolution kinetics

The basaltic glass dissolution rate was simulated according to the transition state theory and using the far-from-equilibrium rate expression from Gíslason and Oelkers (2003),

$$r_{+,geo} = A_{geo}k_{geo}e^{(-E_A/RT)}\left(a^3_{H^+}/a_{Al^{3+}}\right)^{1/3}(1 - Q/K) \qquad (1)$$

where $r_{+,geo}$ is the geometric surface normalized dissolution rate, A_{geo} the geometric reactive surface area taken to be 250 cm^2/g, and k_{geo} and E_A are the rate constant and activation energy taken to be $10^{-5.6}$ and 25.5 kJ mol^{-1}, respectively (Gíslason and Oelkers, 2003). The term $(1 - Q/K)$ represents the chemical affinity describing the change of the rate when approaching equilibrium, with Q/K the saturation state of the basaltic glass. The saturation state was calculated assuming the primary phase to be represented by a leached layer approximated by an amorphous gel consisting of Al-hydroxide and amorphous silica (Oelkers and Gíslason, 2001).

The surface area of the basaltic glass as a function of reaction time was modeled assuming spherical particles and is given by,

$$A_{(t)} = \left(m_{(t)}/m_{(0)}\right)^{2/3}A_{(0)} \qquad (2)$$

where $m_{(t)}$ and $m_{(0)}$ are the moles at time-t and initial moles of basaltic glass at time-0 and $A_{(0)}$ is the initial geometric surface area at time-0. The exponent value of 2/3 corresponds to a monodisperse population of isomeric shaped spheres or cubes dissolving uniformly over their entire surface area (e.g. Larsen and Postma, 2001).

2.3. Thermodynamic dataset

Mineral saturations, ion activities and chemical speciation were calculated using PHREEQC version 2.17.5 (Parkhurst and Appelo, 1999) and the phreeqc.dat thermodynamic database that was updated for the present study with respect to the secondary minerals of interest.

Table 4
The dissolution reactions for minerals included in the reaction path calculations.

Mineral	Dissolution reactions
Carbonates	
Calcite	$CaCO_3 + H^+ = Ca^{2+} + HCO_3^-$
Siderite	$FeCO_3 + H^+ = Fe^{2+} + HCO_3^-$
Magnesite	$MgCO_3 + H^+ = HCO_3^- + Mg^{2+}$
Ankerite	$CaFe(CO_3)_2 + 2H^+ = Ca^{2+} + Fe^{2+} + 2HCO_3^-$
Dolomite	$CaMg(CO_3)_2 + 2H^+ = Ca^{2+} + 2HCO_3^- + Mg^{2+}$
$Ca_{0.25}Mg_{0.50}Fe_{0.25}$ carbonate	$Ca_{0.25}Mg_{0.50}Fe_{0.25}CO_3 + H^+ = 0.25Ca^{2+} + 0.5\ Mg^{2+} + 0.25Fe^{2+} + HCO_3^-$
$Ca_{0.25}Mg_{0.25}Fe_{0.50}$ carbonate	$Ca_{0.25}Mg_{0.25}Fe_{0.50}CO_3 + H^+ = 0.25Ca^{2+} + 0.25\ Mg^{2+} + 0.5Fe^{2+} + HCO_3^-$
$Mg_{0.25}Fe_{0.75}$ carbonate	$Mg_{0.25}Fe_{0.75}CO_3 + H^+ = 0.75Fe^{2+} + 0.25\ Mg^{2+} + HCO_3^-$
$Mg_{0.50}Fe_{0.50}$ carbonate	$Mg_{0.50}Fe_{0.50}CO_3 + H^+ = 0.5Fe^{2+} + 0.5\ Mg^{2+} + HCO_3^-$
$Mg_{0.75}Fe_{0.25}$ carbonate	$Mg_{0.75}Fe_{0.25}CO_3 + H^+ = 0.25Fe^{2+} + 0.75\ Mg^{2+} + HCO_3^-$
Silica polymorphs	
Quartz	$SiO_2 + 2H_2O = H_4SiO_4^0$
Amorphous silica	$SiO_2 + 2H_2O = H_4SiO_4^0$
Moganite	$SiO_2 + 2H_2O = H_4SiO_4^0$
Chalcedony	$SiO_2 + 2H_2O = H_4SiO_4^0$
Zeolites	
Analcime	$Na_{0.96}Al_{0.96}Si_{2.04}O_6 \cdot 1.02H_2O + 4.98H_2O = 0.96Al(OH)_4^- + 2.04H_4SiO_4^0 + 0.96Na^+$
Chabazite-Ca	$CaAl_2Si_4O_{12} \cdot 6H_2O + 6H_2O = 2Al(OH)_4^- + Ca^{2+} + 4H_4SiO_4^0$
Thomsonite	$Ca_2NaAl_5Si_5O_{20} \cdot 6H_2O + 14H_2O = 5Al(OH)_4^- + 2Ca^{2+} + 5H_4SiO_4^0 + Na^+$
Heulandite-Ca	$CaAl_2Si_7O_{18} \cdot 6H_2O + 12H_2O = 2Al(OH)_4^- + Ca^{2+} + 7H_4SiO_4^0$
Stilbite-Ca	$CaAl_2Si_7O_{18} \cdot 7H_2O + 11H_2O = 2Al(OH)_4^- + Ca^{2+} + 7H_4SiO_4^0$
Scolecite	$CaAl_2Si_3O_{10} \cdot 3H_2O + 7H_2O = 2Al(OH)_4^- + Ca^{2+} + 3H_4SiO_4^0$
Natrolite	$Na_2Al_2Si_3O_{10} \cdot 2H_2O + 8H_2O = 2Al(OH)_4^- + 3H_4SiO_4^0 + 2Na^+$
Mesolite	$Ca_{0.666}Na_{0.666}Al_2Si_3O_{10} \cdot 2.667H_2O + 7.333H_2O = 2Al(OH)_4^- + 0.667Ca^{2+} + 3H_4SiO_4^0 + 0.666Na^+$
Mordenite-Ca	$Ca_{0.5}AlSi_5O_{12} \cdot 4H_2O + 8H_2O = Al(OH)_4^- + 0.5Ca^{2+} + 5H_4SiO_4^0$
Phyllosilicates	
Ca-Beidellite	$Ca_{0.165}Al_2[Al_{0.33}Si_{3.67}]O_{10}(OH)_2 + 12H_2O = 2.33Al(OH)_4^- + 0.165Ca^{2+} + 2H^+ + 3.67H_4SiO_4^0$
Mg-Beidellite	$Mg_{0.165}Al_2[Al_{0.33}Si_{3.67}]O_{10}(OH)_2 + 12H_2O = 2.33Al(OH)_4^- + 2H^+ + 3.67H_4SiO_4^0 + 0.165\ Mg^{2+}$
Ca-nontronite	$Ca_{0.165}{Fe^{3+}}_2[Al_{0.33}Si_{3.67}]O_{10}(OH)_2 + 12H_2O = 0.33Al(OH)_4^- + 0.165Ca^{2+} + 2Fe(OH)_4^- + 2H^+ + 3.67H_4SiO_4^0$
Mg-nontronite	$Mg_{0.165}{Fe^{3+}}_2[Al_{0.33}Si_{3.67}]O_{10}(OH)_2 + 12H_2O = 0.33Al(OH)_4^- + 2Fe(OH)_4^- + 2H^+ +$ $3.67H_4SiO_4^0 + 0.165\ Mg^{2+}$
Ca-saponite	$Ca_{0.167}Mg_3[Al_{0.33}Si_{3.67}]O_{10}(OH)_2 + 6H^+ + 4H_2O = 0.33Al(OH)_4^- + 0.165Ca^{2+} + 3.67H_4SiO_4^0 + 3\ Mg^{2+}$
Mg-saponite	$Mg_{0.165}Mg_3[Al_{0.33}Si_{3.67}]O_{10}(OH)_2 + 6H^+ + 4H_2O = 0.33Al(OH)_4^- + 3.67H_4SiO_4^0 + 3.165\ Mg^{2+}$
Ca–(Mg)–Fe smectite[a]	$K_{0.03}Na_{0.01}Ca_{0.18}Mg_{0.08}{Fe^{2+}}_{0.23}{Fe^{3+}}_{0.44}Al_{1.33}[Al_{0.33}Si_{3.67}]O_{10}(OH)_2 + 11.08H_2O = 1.66Al(OH)_4^-$ $+ 0.18Ca^{2+} + 0.23Fe^{2+} + 0.44Fe(OH)_4^- + 3.67H_4SiO_4^0 + 0.03\ K^+ + 0.08\ Mg^{2+} + 0.01Na^+ + 1.08H^+$
Mg-clay[b]	$Ca_{0.04}Mg_{3.01}[Al_{0.1}Si_{3.9}]O_{10}(OH)_2 + 6H^+ + 4H_2O = 0.1Al(OH)_4^- + 0.04Ca^{2+} + 3.9H_4SiO_4^0 + 3.01\ Mg^{2+}$
Ca–Fe clay[b]	$Na_{0.02}Ca_{0.4}Mg_{0.09}{Fe^{3+}}_{2.00}[Al_{1.00}Si_{3.00}]O_{10}(OH)_2 + 12H_2O = Al(OH)_4^- + 0.4Ca^{2+} + 2Fe(OH)_4^- + 2H^+$ $+ 3H_4SiO_4^0 + 0.09\ Mg^{2+} + 0.02Na^+$
Ca–Mg–Fe clay 1[c]	$K_{0.03}Na_{0.05}Ca_{0.13}Mg_{0.81}{Fe^{2+}}_{0.71}Al_{0.9}[Al_{0.08}Si_{3.92}]O_{10}(OH)_2 + 2.4H^+ + 7.6H_2O = 0.98Al(OH)_4^- + 0.13Ca^{2+}$ $+ 0.71Fe^{2+} + 3.92H_4SiO_4^0 + 0.03\ K^+ + 0.81\ Mg^{2+} + 0.05Na^+$
Ca–Mg–Fe clay 2[c]	$K_{0.01}Na_{0.02}Ca_{0.25}Mg_{2.16}{Fe^{2+}}_{0.78}Al_{0.09}[Al_{0.68}Si_{3.32}]O_{10}(OH)_2 + 5.64H^+ + 4.36H_2O = 0.77Al(OH)_4^-$ $+ 0.25Ca^{2+} + 0.78Fe^{2+} + 3.32H_4SiO_4^0 + 0.01\ K^+ + 2.16\ Mg^{2+} + 0.02Na^+$
Ca–Mg–Fe clay 3[d]	$K_{0.02}Na_{0.10}Ca_{0.26}Mg_{1.27}{Fe^{2+}}_{1.91}Al_{0.02}[Al_{1.06}Si_{2.94}]O_{10}(OH)_2 + 5.92H^+ + 4.08H_2O = 1.08Al(OH)_4^-$ $+ 0.26Ca^{2+} + 1.91Fe^{2+} + 2.94H_4SiO_4^0 + 0.02\ K^+ + 1.27\ Mg^{2+} + 0.1Na^+$
Ca–Mg–Fe clay 4[e]	$K_{0.05}Na_{0.03}Ca_{0.18}Mg_{1.41}{Fe^{2+}}_{1.78}Al_{0.05}[Al_{0.97}Si_{3.03}]O_{10}(OH)_2 + 5.8H^+ + 4.2H_2O = 1.02Al(OH)_4^-$ $+ 0.18Ca^{2+} + 1.78Fe^{2+} + 3.03H_4SiO_4^0 + 0.05\ K^+ + 1.41\ Mg^{2+} + 0.03Na^+$
Celadonite natural[e]	$K_{0.88}Na_{0.02}Ca_{0.02}Mg_{0.50}{Fe^{2+}}_{1.02}Al_{0.68}[Al_{0.02}Si_{3.98}]O_{10}(OH)_2 + 3.28H^+ + 6.72H_2O = 0.7Al(OH)_4^-$ $+ 0.02Ca^{2+} + 1.02Fe^{2+} + 3.98H_4SiO_4^0 + 0.88\ K^+ + 0.5\ Mg^{2+} + 0.02Na^+$
Celadonite-Fe	$KFeAlSi_4O_{10}(OH)_2 + 2H^+ + 8H_2O = Al(OH)_4^- + Fe^{2+} + 4H_4SiO_4 + K^+$
Chlorite	$Mg_6Si_4O_{10}(OH)_8 + 12H^+ = 2H_2O + 4H_4SiO_4 + 6Mg^{2+}$
Hydrated Al–silicates	
Kaolinite	$Al_2Si_2O_5(OH)_4 + 7H_2O = 2Al(OH)_4^- + 2H^+ + 2H_4SiO_4^0$
Imogolite (natural gel)	$Al_2SiO_3(OH)_4 + 5H_2O = 2Al(OH)_4^- + 2H^+ + H_4SiO_4^0$
Allophane Al/Si 2.02	$Al_2O_3SiO_2 \cdot 2.53H_2O + 4.47H_2O = 2Al(OH)_4^- + 2H^+ + H_4SiO_4^0$

(*continued on next page*)

Table 4 (*continued*)

Mineral	Dissolution reactions
Allophane Al/Si 1.64	$Al_2O_3(SiO_2)_{1.22}{\cdot}2.5H_2O + 4.94H_2O = 2Al(OH)_4^- + 2H^+ + 1.22H_4SiO_4^0$
Allophane Al/Si 1.26	$Al_2O_3(SiO_2)_{1.59}{\cdot}2.5H_2O + 5.55H_2O = 2Al(OH)_4^- + 2H^+ + 1.59H_4SiO_4^0$
Leached BG layer[f]	$SiAl_{0.35}O_2(OH)_{1.05} + 2.35H_2O = H_4SiO_4^0 + 0.35Al(OH)_4^- + 0.35H^+$
Al- and Fe-oxyhydroxides	
Gibbsite	$Al(OH)_3 + H_2O = Al(OH)_4^- + H^+$
Goethite	$FeOOH + 2H_2O = Fe(OH)_4^- + H^+$
Ferrihydrite (2-line)	$Fe(OH)_3 + H_2O = Fe(OH)_4^- + H^+$

[a] CO_2–water–basalt experiments from Gysi and Stefánsson (2011).
[b] Natural clay mixtures from Crovisier et al. (1992).
[c] Natural di-/trioctahedral smectites from Rogers et al. (2006).
[d] Natural di-/trioctahedral smectites from Neuhoff et al. (2006).
[e] Natural clay mixtures from Neuhoff et al. (1999).
[f] Hydrated basaltic glass (BG) formula derived by addition of $Al(OH)_3$ and SiO_2.

The approach adopted was to critically select Gibbs energy values (ΔG) for key aqueous species and minerals in order to calculate the respective mineral solubility constants.

The reactions have been expressed in terms of dissolution reactions (Table 4) using the predominant aqueous species in natural waters associated with basalts at <100 °C (Stefánsson et al., 2001). However, the pH range of the water under study varied between ~4 and >8 and so does the activity of many of the predominant aqueous species of given components in water. This together with uncertainties associated with the thermodynamic data can lead to significant errors in the calculated reaction quotients of the mineral dissolution reactions and therefore the aqueous species written in the reactions must be selected carefully in order to avoid species with very low activities. The key aqueous species selected for the calculation of the Gibbs energy of the mineral dissolution reactions include H_2O, H^+, $Al(OH)_4^-$, $H_4SiO_4^0$, Mg^{2+}, Ca^{2+}, Na^+, K^+, Fe^{2+}, $Fe(OH)_4^-$ and HCO_3^-, and were selected from Hill (1990), the SUPCRT92, slop98.dat database (Johnson et al., 1992), Diakonov et al. (1999), Gunnarsson and Arnórsson (2000), Bénézeth et al. (2001) and Palmer et al. (2001) (Appendix A).

The standard thermodynamic properties of secondary minerals were selected or calculated based on data given by Robie et al. (1979), Richet et al. (1982), Verdes (1990), Hemingway et al. (1991), Verdes et al. (1992), Su and Harsh (1994, 1998), Robie and Hemingway (1995), Gíslason et al. (1997), Holland and Powell (1998), Heaney and Post (2001), Neuhoff (2000), Majzlan et al. (2004) and Neuhoff et al. (2004) (Appendix B).

The standard state adopted in the present work is that of unit activity for pure minerals and H_2O at any temperature and pressure. The standard state for aqueous species was that of a hypothetical 1 molal solution referenced at infinite dilution at any temperature and pressure. The apparent standard partial molal Gibbs energy was calculated from 25 to 300 °C at water saturation pressure (p_{sat}) according to,

$$\Delta\overline{G}^{\circ}_{T,p,i} = \Delta G^{\circ}_{f,T_r,p_r,i} - S^{\circ}_{T_r,i}(T - T_r) + \int_{T_r}^{T} C^{\circ}_{p,i}dT - T\int_{T_r}^{T} C^{\circ}_{p,i}/TdT + \int_{p_r}^{p} V^{\circ}_{T,i}dP \quad (3)$$

with $\Delta G^{\circ}_{f,T_r,p_r,i}$ the standard state Gibbs free energy of formation, $S^{\circ}_{T_r,i}$ the third law entropy, $C^{\circ}_{p,i}$ the isobaric heat capacity and $V^{\circ}_{T,i}$ molal volume for the ith mineral or aqueous species at the reference temperature (T_r) and pressure (p_r), with T and p the temperature and pressure of interest. The integral for Eq. (3) was solved for aqueous species using the revised HKF equation-of-state (Helgeson et al., 1981; Shock and Helgeson, 1988; Tanger and Helgeson, 1988; Shock et al., 1992) except for the apparent Gibbs energies of $Fe(OH)_4^-$, $Al(OH)_4^-$ and $H_4SiO_4^0$ that were retrieved from solubility experiments and water from Hill (1990).

Subsequently, the Gibbs free energy of reactions listed in Table 4 was calculated from:

$$\Delta G^{\circ}_{T,p,r} = \sum_i v_i \Delta\overline{G}^{\circ}_{T,p,i} \quad (4)$$

with v_i the stoichiometric coefficient (positive for products and negative for reactants). The solubility constants were then calculated using,

$$\log K = \frac{\Delta G^{\circ}_{T,p,r}}{-RT\ln(10)} \quad (5)$$

The results are listed in Table 5 as a function of temperature.

2.4. Carbonate and clay solid solutions

The thermodynamic properties and the respective mineral solubilities for carbonate and clay solid solutions were calculated in the present study.

The composition of carbonate solid solutions associated with CO_2–water–basalt interaction was calculated for Ca–Mg–Fe and Mg–Fe carbonates based on the mineralogy from the Disko-Nuussuaq region (West Greenland) consisting of siderite–magnesite carbonate solid solutions and dolomite (Rogers et al., 2006), as well as carbonate compositions observed to form during laboratory experiments. At low temperature, the formation of Mg-carbonates is restricted to the hydrated end-members nesquehonite ($MgCO_3{\cdot}3H_2O$) and hydromagnesite ($(MgCO_3)_4{\cdot}Mg(OH)_2{\cdot}4H_2O$). The presence of those minerals depends also on the CO_2 concentration (Hänchen et al., 2008). Because of the high dehydration

Table 5
Mineral solubility constants (log *K*) calculated from 25 to 300 °C at water saturation pressures using the mineral dissolution reactions listed in Table 4 and data from Appendix A and B.

Mineral	25 °C	50 °C	75 °C	100 °C	125 °C	150 °C	175 °C	200 °C	225 °C	250 °C	275 °C	300 °C
Carbonates												
Calcite	1.91	1.54	1.18	0.83	0.49	0.15	−0.19	−0.53	−0.89	−1.27	−1.69	−2.16
Siderite	−0.76	−1.14	−1.51	−1.85	−2.19	−2.53	−2.86	−3.20	−3.56	−3.94	−4.35	−4.82
Magnesite	2.31	1.69	1.12	0.61	0.13	−0.33	−0.77	−1.20	−1.64	−2.09	−2.57	−3.09
Ankerite	−0.20	−0.84	−1.47	−2.09	−2.70	−3.31	−3.92	−4.56	−5.23	−5.95	−6.75	−7.65
Dolomite	3.35	2.43	1.57	0.76	−0.01	−0.76	−1.51	−2.25	−3.01	−3.82	−4.69	−5.66
$Ca_{0.25}Mg_{0.50}Fe_{0.25}$ carbonate	0.99	0.49	0.03	−0.40	−0.81	−1.21	−1.60	−1.99	−2.38	−2.80	−3.25	−3.74
$Ca_{0.25}Mg_{0.25}Fe_{0.50}$ carbonate	0.22	−0.22	−0.63	−1.02	−1.39	−1.76	−2.12	−2.49	−2.86	−3.26	−3.69	−4.17
$Mg_{0.25}Fe_{0.75}$ carbonate	−0.24	−0.68	−1.09	−1.48	−1.86	−2.22	−2.58	−2.95	−3.32	−3.72	−4.15	−4.63
$Mg_{0.50}Fe_{0.50}$ carbonate	0.47	−0.03	−0.49	−0.92	−1.33	−1.73	−2.12	−2.50	−2.90	−3.31	−3.76	−4.26
$Mg_{0.75}Fe_{0.25}$ carbonate	1.30	0.74	0.22	−0.25	−0.70	−1.12	−1.54	−1.95	−2.36	−2.80	−3.26	−3.77
Silica polymorphs												
Quartz	−3.75	−3.46	−3.21	−2.98	−2.78	−2.61	−2.45	−2.32	−2.21	−2.12	−2.05	−1.99
Amorphous silica	−2.74	−2.56	−2.39	−2.24	−2.10	−1.98	−1.88	−1.79	−1.72	−1.67	−1.62	−1.60
Moganite	−2.88	−2.72	−2.58	−2.46	−2.34	−2.24	−2.15	−2.06	−1.99	−1.92	−1.85	−1.79
Chalcedony[a]	−3.58	−3.30	−3.05	−2.84	−2.66	−2.49	−2.35	–	–	–	–	–
Zeolites												
Analcime	−15.46	−14.49	−13.63	−12.87	−12.19	−11.60	−11.09	−10.67	−10.35	−10.13	−10.03	−10.05
Chabazite-Ca	−30.90	−29.04	−27.41	−25.99	−24.76	−23.73	−22.89	−22.26	−21.83	−21.63	−21.69	−22.00
Thomsonite	−60.93	−57.71	−54.85	−52.33	−50.11	−48.22	−46.64	−45.45	−44.61	−44.24	−44.36	−45.02
Heulandite-Ca	−42.22	−39.59	−37.26	−35.20	−33.40	−31.85	−30.54	−29.50	−28.70	−28.18	−27.95	−28.01
Stilbite-Ca	−42.41	−39.76	−37.40	−35.31	−33.45	−31.84	−30.47	−29.36	−28.48	−27.88	−27.56	−27.53
Scolecite	−29.14	−27.55	−26.15	−24.93	−23.86	−22.95	−22.20	−21.64	−21.25	−21.07	−21.11	−21.40
Natrolite	−26.53	−24.68	−23.04	−21.59	−20.29	−19.16	−18.19	−17.41	−16.80	−16.39	−16.21	−16.26
Mesolite	−28.26	−26.59	−25.11	−23.81	−22.67	−21.69	−20.86	−20.23	−19.76	−19.51	−19.48	−19.68
Mordenite-Ca	−29.89	−27.94	−26.21	−24.68	−23.33	−22.15	−21.13	−20.29	−19.60	−19.08	−18.73	−18.56
Phyllosilicates												
Ca-Beidellite	−47.60	−44.46	−41.80	−39.53	−37.58	−35.93	−34.55	−33.44	−32.57	−31.99	−31.68	−31.67
Mg-Beidellite	−49.29	−46.04	−43.25	−40.84	−38.75	−36.96	−35.42	−34.16	−33.14	−32.41	−31.95	−31.79
Ca-nontronite	−56.82	−53.42	−50.49	−47.93	−45.67	−43.67	−41.90	−40.34	−38.98	−37.83	−36.88	−36.14
Mg-nontronite	−58.51	−55.02	−52.01	−49.38	−47.06	−45.00	−43.18	−41.58	−40.18	−38.98	−38.00	−37.23
Ca-saponite	20.34	17.84	15.76	13.99	12.47	11.13	9.92	8.80	7.73	6.69	5.63	4.55
Mg-saponite	18.88	16.46	14.44	12.73	11.26	9.96	8.80	7.71	6.68	5.67	4.63	3.59
Ca–(Mg)–Fe smectite	−42.63	−39.96	−37.67	−35.69	−33.95	−32.45	−31.16	−30.10	−29.23	−28.60	−28.20	−28.04
Mg-clay natural	21.41	18.98	16.96	15.25	13.77	12.48	11.32	10.26	9.25	8.27	7.29	6.31
Ca–Fe clay natural	−60.54	−57.21	−54.34	−51.85	−49.65	−47.72	−46.02	−44.57	−43.32	−42.31	−41.56	−41.06
Ca–Mg–Fe clay 1	−10.59	−10.27	−9.97	−9.69	−9.44	−9.23	−9.08	−9.02	−9.03	−9.15	−9.40	−9.78
Ca–Mg–Fe clay 2	13.04	11.02	9.33	7.90	6.66	5.56	4.55	3.59	2.65	1.68	0.67	−0.42
Ca–Mg–Fe clay 3	9.24	7.37	5.80	4.47	3.31	2.27	1.31	0.37	−0.56	−1.55	−2.61	−3.77
Ca–Mg–Fe clay 4	8.60	6.80	5.30	4.02	2.91	1.91	0.99	0.09	−0.81	−1.75	−2.77	−3.88
Celadonite natural	−4.53	−4.25	−3.97	−3.71	−3.46	−3.25	−3.09	−3.00	−2.98	−3.06	−3.24	−3.53

Celadonite-Fe	−19.00	−17.76	−16.65	−15.66	−14.79	−14.05	−13.42	−12.93	−12.57	−12.35	−12.30	−12.40
Chlorite	62.52	56.23	50.97	46.52	42.70	39.35	36.37	33.68	31.19	28.84	26.58	24.38
Hydrated Al–silicates												
Kaolinite	−40.63	−38.00	−35.71	−33.72	−31.98	−30.47	−29.16	−28.08	−27.20	−26.54	−26.12	−25.93
Imogolite (natural gel)	−33.74	−31.84	−30.21	−28.82	−27.60	−26.57	–	–	–	–	–	–
Allophane Al/Si 2.02	−36.04	−33.82	−31.92	−30.29	−28.87	−27.66	–	–	–	–	–	–
Allophane Al/Si 1.64	−34.42	−32.42	−30.71	−29.25	−27.98	−26.89	–	–	–	–	–	–
Allophane Al/Si 1.26	−30.64	−28.80	−27.22	−25.87	−24.69	−23.69	–	–	–	–	–	–
Leached BG layer	−8.06	−7.47	−6.97	−6.55	–	–	–	–	–	–	–	–
Al- and Fe-oxyhydroxides												
Gibbsite	−15.18	−14.03	−13.10	−12.33	–	–	–	–	–	–	–	–
Goethite	−21.06	−19.95	−19.01	−18.19	−17.48	−16.83	−16.26	−15.76	−15.30	−14.91	−14.57	−14.30
Ferrihydrite (2-line)	−17.64	−16.75	−15.97	−15.28	−14.65	−14.08	−13.56	−13.08	−12.64	−12.25	−11.92	−11.64

[a] Data taken from Arnórsson et al. (1982).

energy associated to the Mg^{2+} ions and kinetic restrictions, the precipitation of magnesite is inhibited at low temperatures (Saldi et al., 2009). Nevertheless, synthetic carbonate precipitation experiments from Romanek et al. (2009) have shown that Ca–Fe carbonates form preferentially metastable phases at 25 °C with some incorporation of Mg, whereas at 70 °C the Mg ion predominate in the solid solutions. Therefore we chose to estimate the thermodynamic properties of carbonates as a set of Ca–Mg–Fe solid solutions of fixed composition by assuming an ideal solid solution model. The carbonate end-members selected consisted of siderite, calcite and magnesite. The apparent standard partial molal Gibbs energy, entropy and molal volume of the carbonate solid solutions were calculated from ideal mechanical mixing, the configurational entropy and the ideal mole fractions of the end-member carbonates in the carbonate solid solution (Stefánsson, 2001).

The chemical and structural complexity of clay minerals is the cause of the scarce availability of experimentally derived thermodynamic data for these minerals, not to mention the presence of impurities and different hydration states that make the experiments difficult. Several methods have been developed to estimate the thermodynamic properties of clay solid solutions over a wider range of compositions. These estimates consist of either oxide summation techniques (e.g. Tardy and Garrels, 1974, 1976, 1977; Chermak and Rimstidt, 1989) or are based on solubility products of well-crystallized phyllosilicate end-members assuming an ideal solid solution model (Tardy and Fritz, 1981). In the present study, we used a combination of oxide summation techniques that were applied by Vidal and Dubacq (2009) for estimating standard state properties of smectite end-members. Firstly, the Gibbs free energy of formation for anhydrous clay minerals (ΔG_f°) was calculated at 1 bar and 25 °C as described in Chermak and Rimstidt (1989) by summing the contribution of each polyhedral units (g_i) from their regressed database consisting of $^{(4,6)}Al_2O_3$, $^{(6)}Al(OH)_3$, $^{(4)}SiO_2$, $^{(6)}MgO$, $^{(6)}Mg(OH)_2$, $^{(6)}CaO$, $^{(6\text{–}8)}Na_2O$, $^{(8\text{–}12)}K_2O$, H_2O, $^{(6)}FeO$, $^{(6)}Fe(OH)_2$ and $^{(6)}Fe_2O_3$ (numbers in brackets correspond to coordination numbers). The g_i for $^{(6)}Fe(OH)_3$ was calculated in the present study from the ΔG_f° of goethite (Holland and Powell, 1998) and the $^{(6)}Fe_2O_3$ polyhedron mentioned above giving a g_i value of −696.6 kJ mol^{-1}. Secondly, the third law entropy ($S°$) was retrieved using the approach and dataset from Holland (1989). The $(S - V)_{H_2O}$, corresponding to the entropy (S) and volume (V) of the mineral forming oxide component (Holland, 1989), was adjusted to 20 J K^{-1} mol^{-1} in order achieve calculated $S°$ for Fe-celadonite, phlogopite, muscovite and pyrophyllite with an error <1% compared to the thermodynamic database from Holland and Powell (1998). The molar volume ($V°$) of smectites was assumed to correspond to the values of phlogopite and muscovite for tri- and diocthaedral smectites, respectively. Thirdly, the heat capacity equation (C_p) was retrieved as a function of temperature using the method and regressed dataset of Berman and Brown (1985). The overall accuracy for the estimated apparent Gibbs energy from 25 to 300 °C for clay mineral solid solutions have been assessed by calculating the values for Fe-celadonite, chlorite, phlogopite, muscovite, pyrophyllite and talc from the Holland and Powell (1998) database. The difference between the estimated and calculated values were <0.75% with absolute differences ranging between ~90 and 50,630 J mol^{-1} indicating that this approach is reasonable for the purpose of our study.

3. CO_2–WATER–BASALT INTERACTION

3.1. Low CO_2 systems at 25 °C

The results of the reaction path simulations between basaltic glass and dilute waters both open and closed to atmospheric CO_2 are shown in Figs. 1–3.

The modeled pH was found to increase with increasing reaction progress. However, the exact pH changes were sensitive to the initial water alkalinity and pH. For systems in contact with atmospheric CO_2, the pH rose rapidly to above 7 and levelled off between 7.5 and 8. This is in good agreement with observed pH values of natural surface waters in contact with basaltic rocks (Gíslason and Eugster, 1987b; Gíslason et al., 1996; Stefánsson and Gíslason, 2001). For waters sealed off from atmospheric CO_2, the pH rose eventually reaching values between 10 and 11. This is in agreement with pH values observed in basalt-associated spring and ground waters, whose evolution presumably occurred under closed-system with initial CO_2 close to atmospheric values (Gíslason and Eugster, 1987b; Gíslason et al., 1996; Stefánsson and Gíslason, 2001). The elemental concentrations and secondary minerals formed were primarily dependent on water pH and extent of reaction. Most elements were incorporated at some stage into secondary minerals, reducing their mobility. Several secondary minerals listed in Table 4 were combined and variations tested in order to achieve the resulting reaction path with the detailed mineralogy given in Fig. 3. The overall reaction progress of surface water reacting with basalt can be divided into three main stages (Fig. 3). At low reaction progress (Stage I), the main secondary minerals formed consist of simple Al- and Fe-oxyhydroxides limiting the availability of Fe and Al. With increasing reaction progress (Stage II) Al–Si minerals (allophane, imogolite and/or kaolinite) and Mg–Fe clays limit the availability of Mg, Fe, Al and Si with eventually some calcite and zeolites forming. Finally, at high reaction progress (Stage III) and alkaline pH

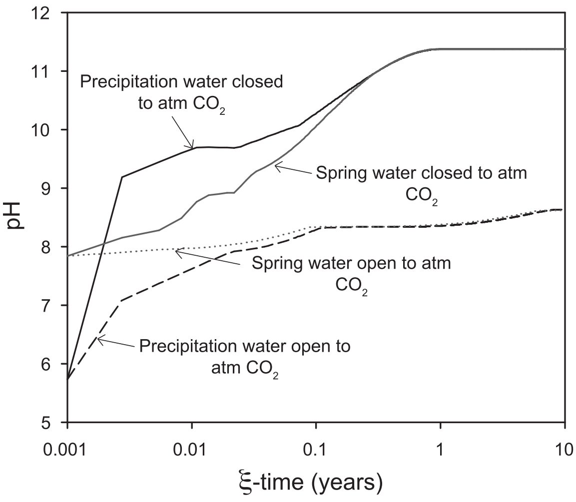

Fig. 1. The relationship between pH and ξ (reaction progress)-time in years for natural spring water (Vellankatla) and unpolluted precipitation water (Langjökull) open (surface water) and closed (groundwater) to atmospheric CO_2. The calculations were carried out with initial 10 g basaltic glass in 1 kg water at 25 °C.

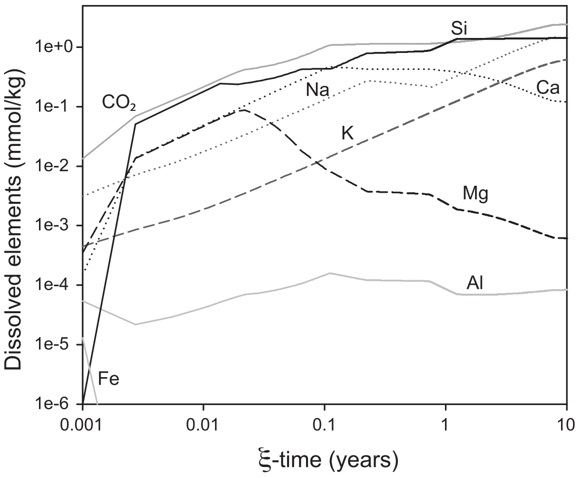

Fig. 2. The solution composition as a function of ξ (reaction progress)-time. The calculations were carried out using natural precipitation water (Langjökull), open to atmospheric CO_2 and with initial 10 g basaltic glass in 1 kg water at 25 °C.

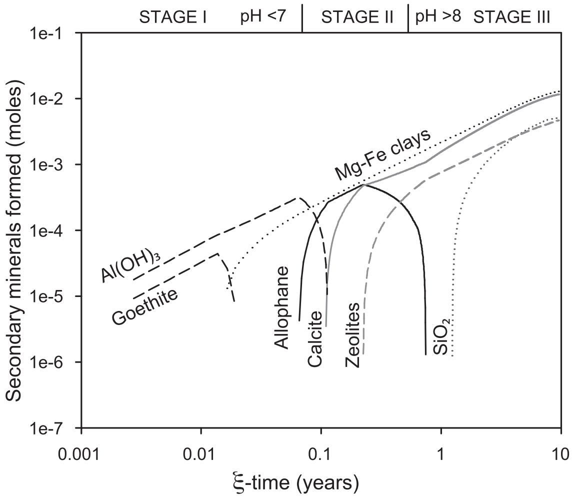

Fig. 3. The secondary mineralogy formed upon ξ (reaction progress)-time. The calculations were carried out using natural precipitation water (Langjökull), open to atmospheric CO_2 and with initial 10 g basaltic glass in 1 kg water at 25 °C. Mg–Fe clays precipitating during the simulations correspond to Mg-saponite and Mg-nontronite, SiO_2 to moganite, $Al(OH)_3$ to gibbsite, allophane to imogolite and allophane (Al/Si = 1.64), and zeolites to thomsonite and analcime.

values the dominant secondary minerals formed were Mg–Fe clays as well as calcite, zeolites and SiO_2-minerals limiting the mobility of Na, Ca and Si. According to the reaction path calculations, the overall mobility of elements was with increasing reaction progress: Al, Fe < Si, Mg, Ca < Na, K.

The above modeled low CO_2–water–basalt interaction reaction paths are very similar to those observed in laboratory experiments and natural systems, i.e. the appearance of simple oxyhydroxides followed by Al–Si minerals like allophane, imogolite and kaolinite, Ca–Mg–Fe smectites and even zeolites and carbonates (Singer, 1974; Wielemaker and Wakatsuki, 1984; Van der Gaast et al., 1986; Crovisier et al., 1992; Nesbitt and Wilson, 1992; Stefánsson and Gíslason, 2001). This results in very low concentrations of Fe and Al particularly and reduced mobility of many other elements like Ca, Mg and Si (Gíslason et al., 1996; Stefánsson and Gíslason, 2001).

3.2. Elevated CO_2 systems at 25–90 °C

The results of the reaction path simulations between basaltic glass with dilute waters initially saturated with 2, 10 and 30 bar CO_2 at 25, 40 and 90 °C are shown in Figs. 4–8. Several secondary minerals listed in Table 4 were combined and variations tested in order to achieve the resulting reaction paths with the detailed mineralogy given in Figs. 5 and 7.

The addition of CO_2 had significant effects on both water and secondary mineral composition as well as mass transfer compared to low CO_2 systems at all temperatures.

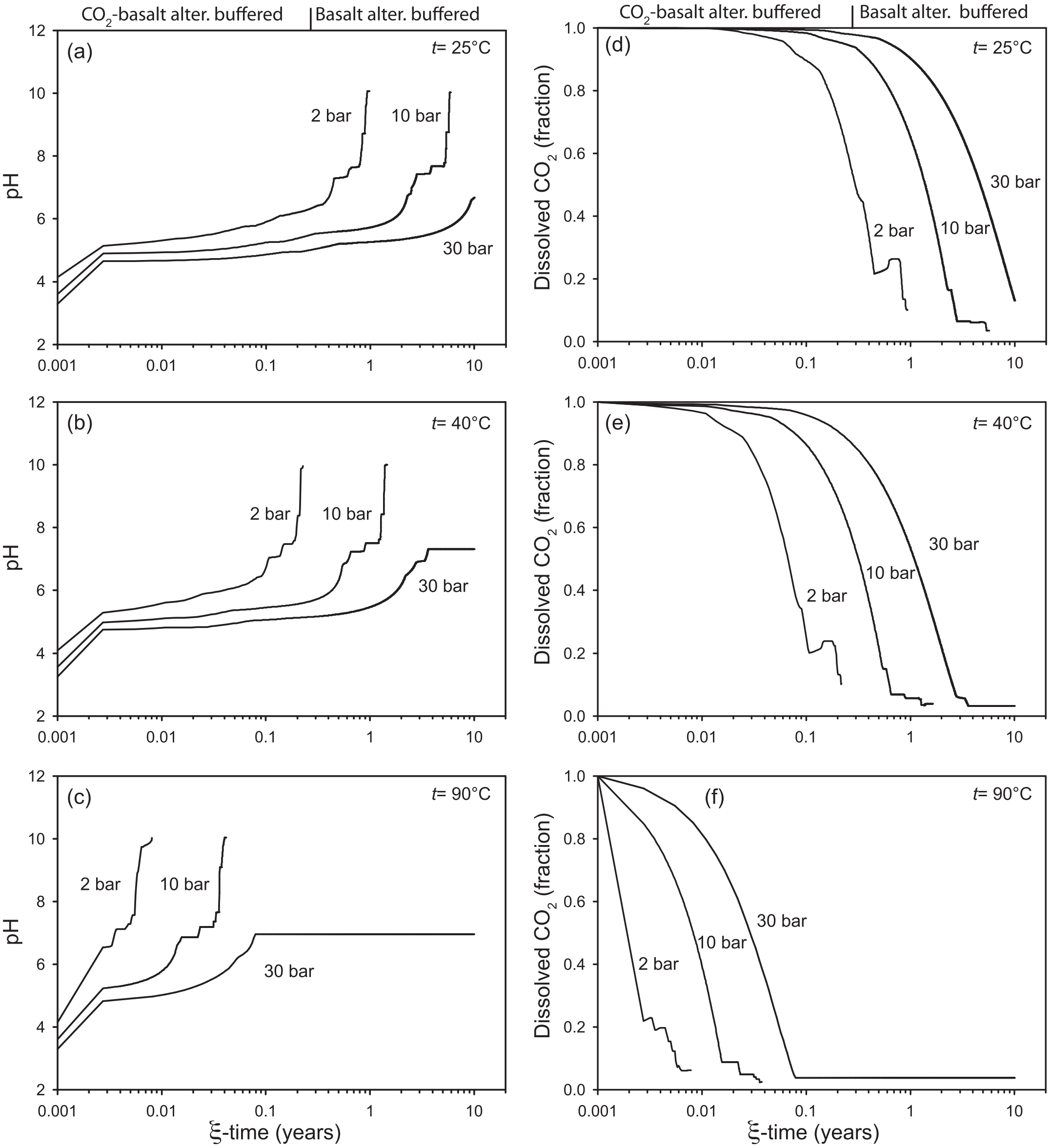

Fig. 4. The changes of pH (a–c) and mole fraction CO_2 (d–f) as a function of ξ (reaction progress)-time at 25, 40 and 90 °C. The calculations were carried out using spring water (Vellankatla) initially saturated with 2, 10 and 30 bar CO_2 and 200 g basaltic glass in 1 kg water. Also shown is the CO_2–basalt alteration buffered system at pH <6.5 and basalt alteration buffered system at pH >8 for 2 bar initial CO_2 at 25 °C.

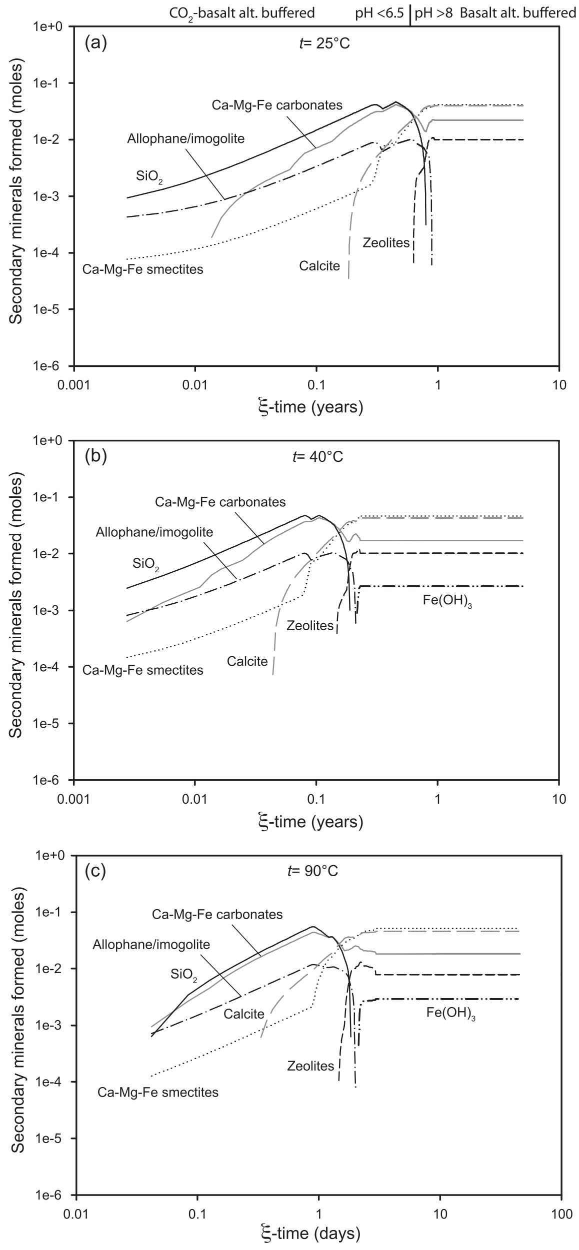

Fig. 5. The secondary mineralogy formed upon ξ (reaction progress)-time at (a) 25, (b) 40 and (c) 90 °C. The calculations were carried out using spring water (Vellankatla) initially saturated with 2 bar CO_2 and 200 g basaltic glass in 1 kg water. Ca–Mg–Fe smectites correspond to Ca–(Mg)–Fe smectite and Ca–Mg–Fe clay 1, SiO_2 to moganite and zeolites to chabazite, thomsonite and analcime listed in Table 4. Carbonates and Al–Si minerals precipitating during the simulations correspond to the detailed mineralogy shown in Fig. 7.

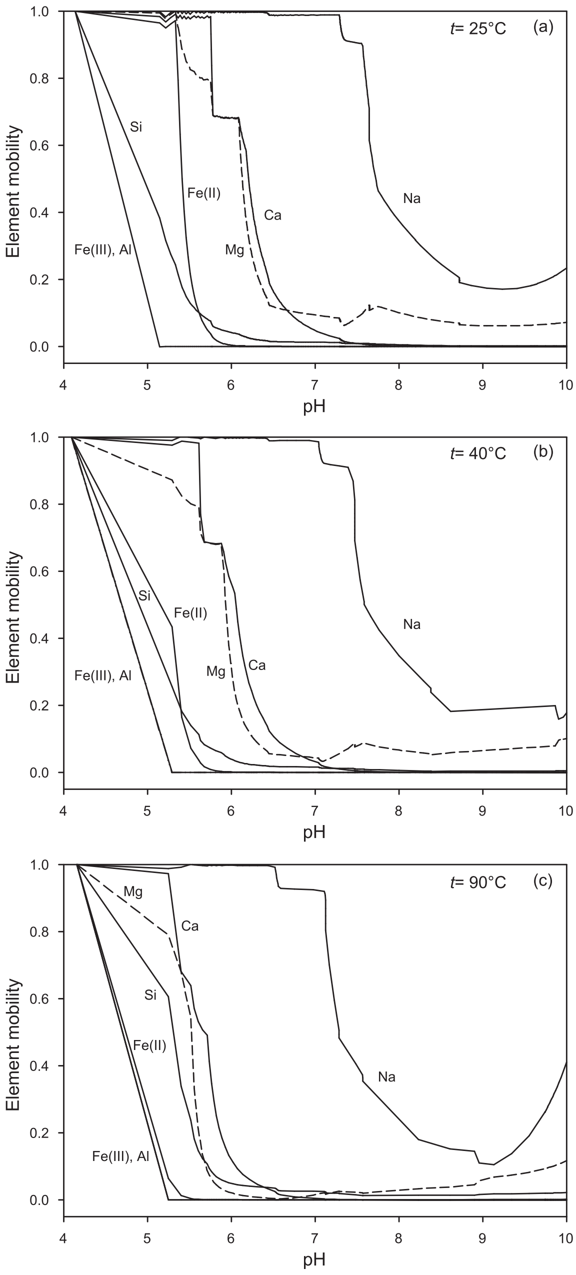

Fig. 6. Element mobility as a function of pH at 25 (a), 40 (b) and 90 °C (c). Calculations were carried out using spring water (Vellankatla) initially saturated with 2 bar CO_2 and 200 g basaltic glass in 1 kg water.

Initially, the pH increased to 4.5–6 depending on the initial CO_2 partial pressure (Fig. 4). Under these conditions, the pH was then buffered by the CO_2 concentration and ionization, proton consumption upon basaltic glass dissolution and proton consumption/release upon secondary mineral precipitation. Upon quantitative carbonate mineralization (Fig. 5) and subsequent decrease in dissolved CO_2 concentration, the pH rose rapidly upon basalt dissolution to values above 8. The time and quantity of basaltic glass dissolution required to quantitatively mineralize the CO_2 was dependent on the initial CO_2 content of the system and the dissolution rate of the basaltic glass, which in turn is pH dependent (Gíslason and Oelkers, 2003). Based on these finding, the water–basalt interaction was divided into two categories. At pH <6.5 the system refers to CO_2–basalt alteration buffered systems whereas at pH >8 it refers to basalt alteration buffered systems (Fig. 4).

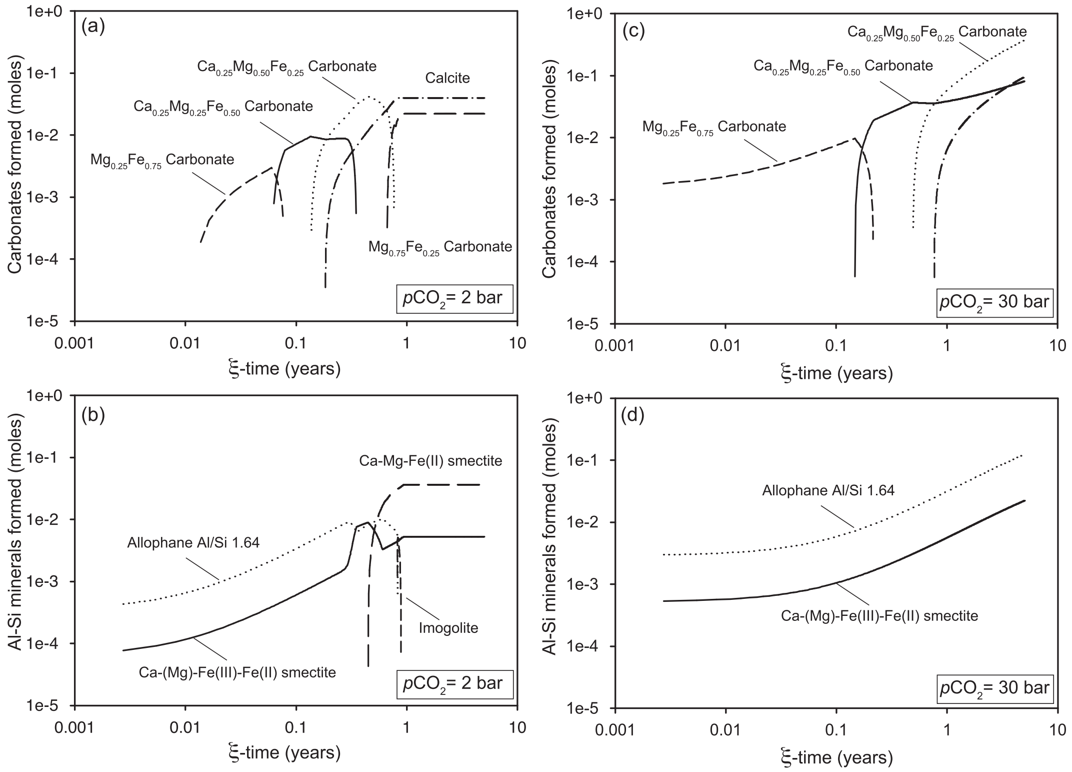

Fig. 7. Mass of carbonates and clays formed as a function of ξ (reaction progress)-time at 25 °C. The calculations were carried out using spring water (Vellankatla) initially saturated with 2 (a and b) and 30 bar (c and d) CO_2 and 200 g basaltic glass in 1 kg water.

The addition of CO_2 to the water had profound effects on the secondary mineral formation, both in terms of composition and mass, as well as elemental mobility (Figs. 5 and 6). The mobility was retrieved from the ratio of the rock-derived element in solution to the total amount of element released from the basaltic glass,

$$\text{mobility } (\%) = \frac{(m_{i(t)} - m_{i(0)}) \cdot m_w}{v_i \cdot n_{bg(t)}} \qquad (6)$$

with $m_{i(t)}$ and $m_{i(0)}$ the concentration of cation (i) in solution (mol/kg) at time-t and time-0, respectively, m_w the mass of water, v_i the stoichiometric coefficient in the basaltic glass formula and $n_{bg(t)}$ the total moles dissolved basaltic glass at time-t.

Under elevated CO_2 concentration and pH <6.5, Al and Si were quantitatively removed into simple oxides and hydroxides, namely $Al(OH)_3$ and/or Al–Si minerals (allophane/imogolite), and SiO_2-minerals. On the other hand, the mobility of Fe was dependent on its oxidation state. Assuming the redox conditions to be controlled by the supply of Fe from the basalt dissolution and consumption by secondary minerals, the Fe(II) oxidation state predominates. This resulted in formation of Ca–Mg–Fe(II) containing carbonates and some Ca–(Mg)–Fe(II)–Fe(III) containing smectites reducing the mobility of Fe, Mg and Ca. Calcite was not observed to be stable under these conditions. The exact composition of the carbonates formed in the reaction path calculations was primarily dependent on the mobility of Ca, Mg and Fe, the oxidation state of Fe and the carbonate and clays solubilities. In turn, the mobility of the elements was largely influenced by the pH. At pH <6.5 (CO_2–basalt alteration buffered conditions) some of the Mg, Fe and Ca were incorporated into smectites, however, the mass of smectites formed was limited by the availability of Al and Si (Fig. 6). This resulted in Mg, Fe and Ca being available for carbonate mineralization and formation of mixed Ca–Mg–Fe carbonates (Fig. 7). At higher reaction progress and pH >8 the systems evolved towards the basalt alteration buffered step with Ca–Mg–Fe(II) smectites, Fe-oxyhydroxides and zeolites becoming the dominant secondary minerals. This resulted in reduced mobility of Mg, Fe and Ca and undersaturation of Mg–Fe containing carbonates. Calcite, on the other hand was observed to be stable under these conditions.

Increased temperature did not have fundamental effects on neither the secondary mineralogy nor the water composition. However, some significant changes are seen. In particular, the rate of basaltic glass dissolution increases with increasing temperature and consequently, mass transfer becomes much faster shifting the pH, dissolved CO_2 and secondary minerals formed with time (Figs. 4 and 5). In addition, the amount of Ca–Mg–Fe carbonates formed relative to SiO_2 during the CO_2–basalt alteration buffered step showed an important increase with temperature. The reduced mobility of Fe(II), Ca, and Mg was then shifted to lower pH values due to the quantitatively higher carbonate mineralization (Fig. 6). The exact composition of Al–Si containing minerals changed as well, with for example allophane and/or Al-hydroxides being replaced by other simple Al–Si minerals like imogolite or possibly kaolinite.

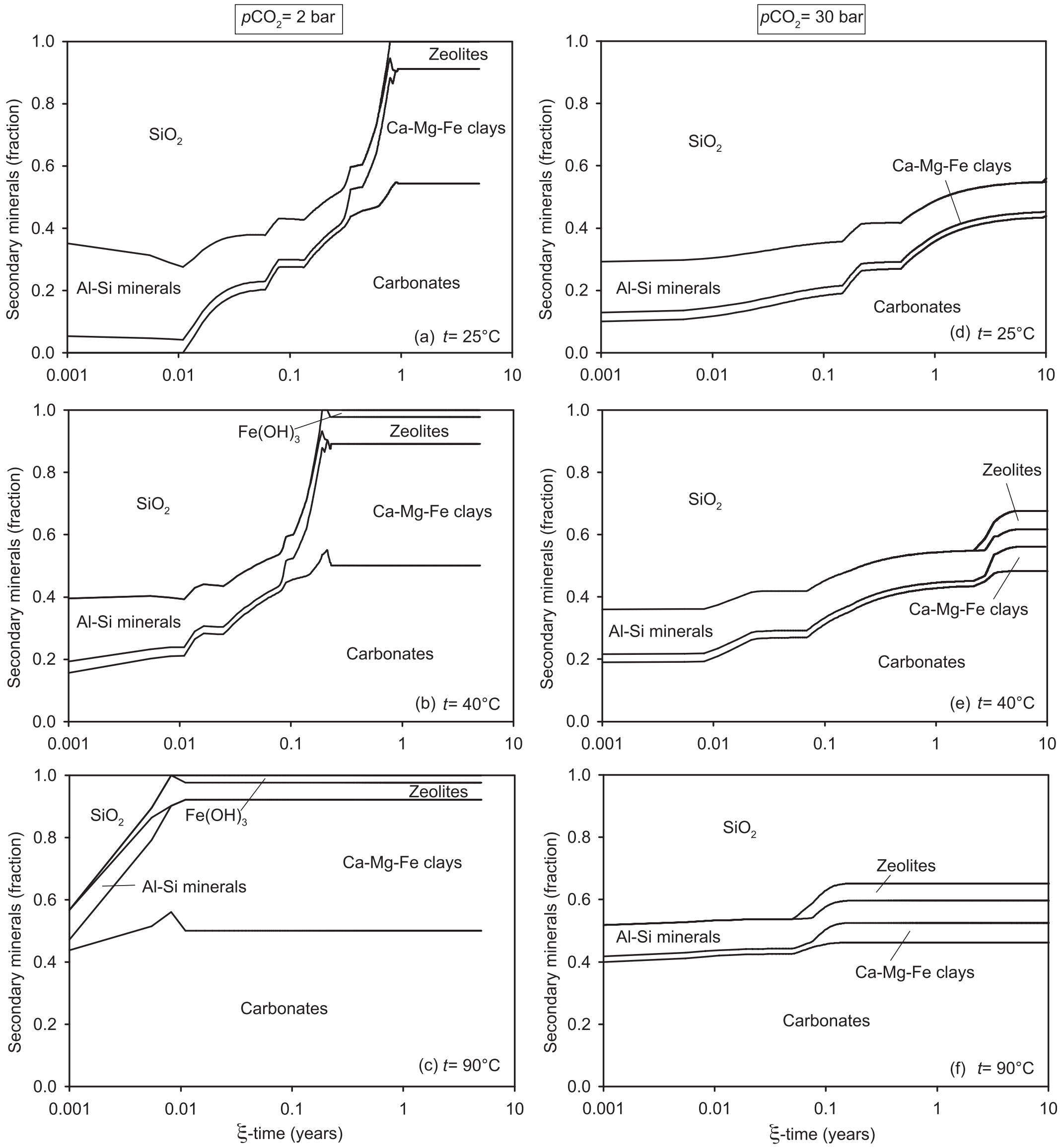

Fig. 8. Mole fraction of secondary minerals formed as a function of ξ (reaction progress)-time at 25, 40 and 90 °C. The calculations were carried out using spring water (Vellankatla) initially saturated with 2 (a–c) and 30 bar (d–f) CO_2 and 200 g basaltic glass in 1 kg water.

The relative mole fraction of the secondary minerals formed is shown in Fig. 8 as a function of initial pCO_2 and temperature. The relative importance of SiO_2 minerals and carbonates increased with increasing CO_2 concentration, whereas clays and zeolites became less important. Moreover, the Al–Si mineralogy is less complex under CO_2-rich conditions with simple Al–Si- and SiO_2-minerals predominating and the Ca, Mg and Fe going primarily into carbonates. At low initial pCO_2 and alkaline pH values (pH >8) the secondary mineralogy is more complex with Si, Al, Ca, Mg and Fe being incorporated into Ca–Mg–Fe clays and zeolites as well as calcite mainly. These observations are in very good agreement with natural analogs and experimental observations. The alteration of basalts at low temperature under CO_2 enriched conditions favors the formation of Ca–Mg–Fe containing carbonates and SiO_2 with the presence of some smectites and Al–Si minerals as well as oxyhydroxides (Rogers et al., 2006; Gysi and Stefánsson, 2011). In contrast, basalt alteration associated with neutral to alkaline waters produces typically Ca–Mg–Fe rich clays, Na–Ca zeolites, SiO_2–minerals and calcite (Neuhoff et al., 1999).

3.3. The overall CO_2–water–basalt reaction progress

Fig. 9 shows a schematic overview of the reaction path of CO_2–water–basalt interaction and a basaltic glass vug with the secondary minerals formed as well as the change in quantities and element mobilities as a function of reaction progress at elevated CO_2.

At low reaction progress, the amount of secondary minerals is low, with the mineralization of simple Al–Si and SiO_2 minerals limiting the mobility of Al and Si. The presence of Al–Si and SiO_2 minerals has not been observed to

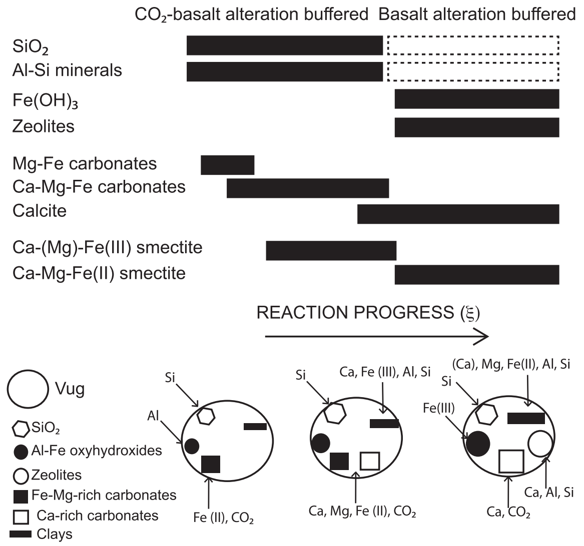

Fig. 9. Schema of secondary mineral sequence formed during CO_2–water–basalt interaction and evolution of a vug upon reaction progress (ξ).

be quantitatively important in laboratory CO_2–water–basalt experiments. Therefore, the presence of these phases may not be explained in terms of secondary mineralization, but rather due to the leaching of the elements from the basaltic glass that progressively becomes enriched in Al and Si and possibly begins to form an altered layer. The system pH was initially buffered at 4.5–6 by CO_2 ionization, basalt dissolution and secondary mineral formation with Fe(II)-carbonate mineralization. With increasing reaction progress, the CO_2 mineralization increases as well as the amount of secondary minerals formed with Ca, Mg and particularly Fe(II) becoming incorporated into carbonates. Calcium and Fe(II) were also mineralized into smectite. The amount of smectites formed was found to be pH dependent, and the oxidation of Fe(II) to Fe(III) becomes more important at pH >5.5 (Gysi and Stefánsson, 2011), favoring the mineralization of Fe (III)-rich smectites and ferrihydrites with increasing pH.

Upon increased basaltic glass dissolution and CO_2-mineralization, the pH increases above 6.5 with SiO_2, Al–Si minerals and Ca–(Mg)–Fe smectites being replaced by zeolites and Ca–Mg–Fe containing smectites reducing the mobility of Al, Si, Mg and Fe leaving Ca the only available cation for carbonate mineralization with calcite becoming the predominant carbonate mineral under alkaline conditions.

The competing reaction for Ca, Mg and Fe between carbonates and clays at low reaction progress, and carbonates, zeolites and clays at high reaction progress determine the stability of carbonate minerals, their compositions as well as the amount of CO_2 getting mineralized. At low reaction progress, Ca–Mg–Fe ions are available for carbonate formation due to the restricted availability of Al and Si by clay mineralization. At high reaction progress, the solubilities and quantity of clays and zeolites determined the Al and Si availability as well as Mg and Fe mobility.

3.4. Comparison with natural and experimental data and computational uncertainties

The reaction path calculations may provide useful information on the overall CO_2–water–basalt reactions including the secondary mineral formation and water composition. However, such calculations are critically dependent on the thermodynamic and kinetic databases applied as well as the system conditions, including initial fluid and rock composition, reactive surface area and the selection of secondary minerals in the calculations. The assumption of instantaneous equilibration and problems associated to mineral precipitation kinetics may further represent a potential source of uncertainty in the calculations, considering that the role of secondary minerals as pH buffers may be important (e.g. Marini et al., 2003). The driving reaction rates allowing to link time to the reaction path may therefore not solely be related to the dissolution mechanisms of the basaltic glass, but also to the secondary mineral precipitation rates. In order to understand the secondary mineral precipitation, more thermodynamic and kinetic data are needed as well as a better understanding of the problems related to nucleation and growth of hydrated crystalline phases and/or mineral solid solutions (e.g. Fritz et al., 2009). Summarizing, changes in all these factors are able to shift the sequence and quantity of secondary minerals formed as well as the reaction progress dependence on time. In addition, the reaction path was dependent on the composition of clays and carbonates as well as the oxidation state of Fe. In order to evaluate the simulated reaction paths, both with respect to secondary mineralogy and water composition, the results were compared with recent experimental results and natural systems.

Water–rock interaction can be viewed as a titration process (e.g. Garrels, 1967; Helgeson et al., 1969) whereas the water with its dissolved acids like CO_2 acts as the acid and the basalt acts as the base by consuming protons and releasing cations upon dissolution. This results in increased cation to proton ratio with increasing reaction progress. Assuming the system to be saturated with particular secondary minerals at a given temperature and pressure, it follows that the cation to proton ratio must be fixed for a given proton concentration given that the bulk system may be in a partial equilibrium between the primary dissolving phase and the secondary minerals precipitating. Taking the pH as a master variable for the "bulk" reaction progress of a given system (primary rock and stable secondary mineral compositions), the slope of the cation to proton ratio as a function of pH must be fixed by the mineral saturation and the overall reaction stoichiometry of the basalt alteration reaction. Therefore, a change in slope of cation to proton ratio as a function of pH indicates either that the overall reaction stoichiometries are shifted due to a change in stable secondary mineral assemblages for a given reaction progress interval and/or to a change in reaction stoichiometry of the primary dissolving phase.

In Figs. 10 and 11 the results of the model calculations are compared with recent CO_2–water–basalt experimental results and with natural low-temperature waters (0–100 °C) associated with basalts in Iceland (Gysi and

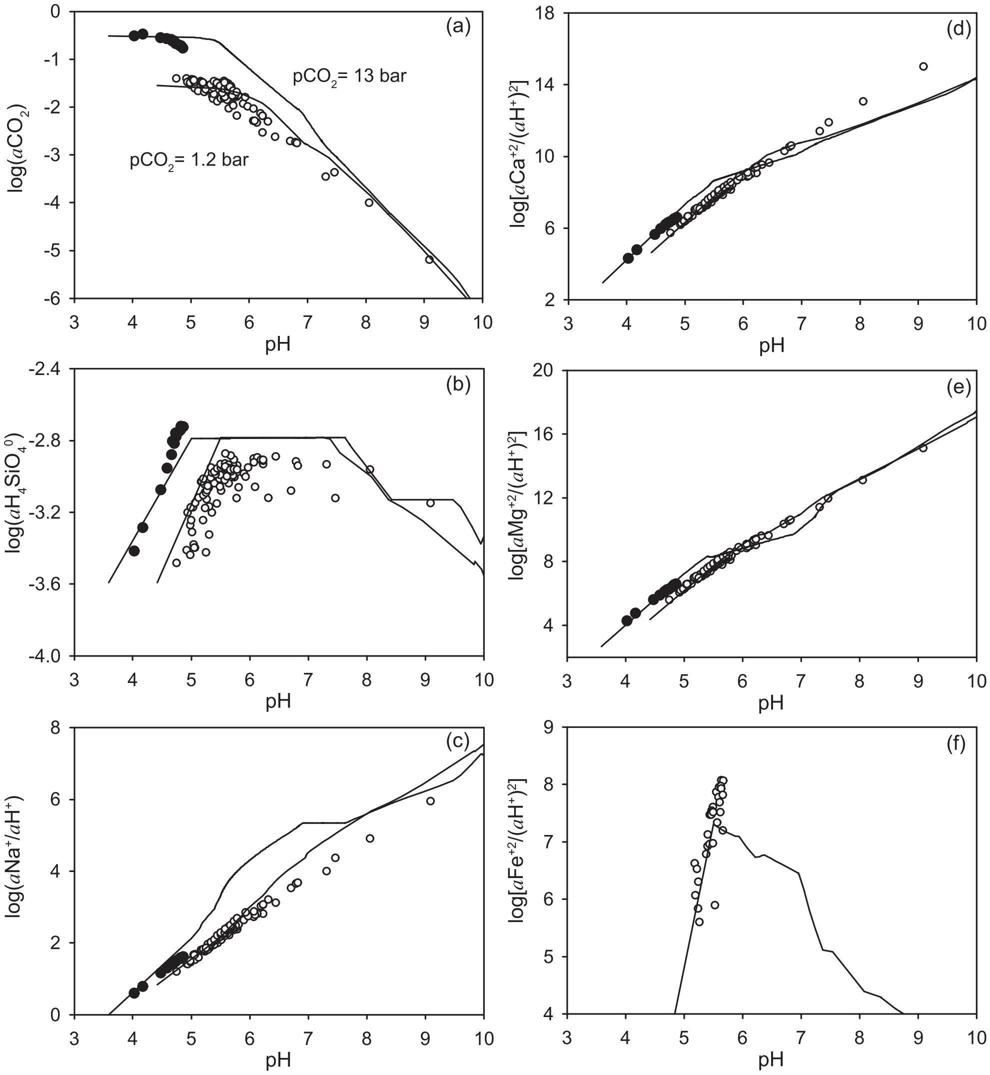

Fig. 10. pH plot of cation to proton activity ratios, CO_2 and $H_4SiO_4{}^0$ and comparison with experimental data. The calculations were carried out at 40 °C using spring water (Vellankatla) initially saturated with 1.2 and 13 bar CO_2 and 200 g basaltic glass in 1 kg water. Black dots indicate experimental solutions at 13 bar pCO_2 and white dots indicate experiments <2 bar pCO_2.

Stefánsson, 2011; Stefánsson and Arnórsson, 2000; Stefánsson et al., 2001), respectively. The calculations were carried out at variable initial CO_2 concentrations. The results show a relatively good agreement between the trends of the model calculations and the natural waters as well as the experimental results. This suggests that the overall stoichiometry of the model is capable of simulating the partial equilibrium conditions for given reaction path intervals of the system both under elevated and low CO_2 conditions. These observations strongly suggest that the alteration process is largely controlled by fine variations in the pH and the pH dependence of secondary mineral composition and saturation. The pH in turn is determined by the balance between the acid supply, extent of reaction and ionization constants of the weak acids and bases in the water.

The activity to proton relationship gives insight into the overall reaction stoichiometry during partial equilibrium conditions controlled by acid supply, primary rock dissolution and secondary mineral formation. However, this relationship is somewhat insensitive to time dependence of mass transfer. In fact, the same trends are observed independent of basaltic glass dissolution rates. To study the effects of mass transfer, the results of the model calculations obtained in the present study were directly compared with the results of batch type reaction experiments. The results are shown in Figs. 12 and 13. A fair agreement is observed between the calculated and the experimentally derived concentrations as a function of time. However, there are three basic problems associated with the model calculations including the true reactive surface area per mass of solution, the formulation of the kinetics as the primary basaltic glass approaches saturation and dissolution mechanism of the basaltic glass.

In our simulations, the basaltic glass dissolution rate normalized to the geometric surface area was used. The modeled results are strongly dependent on the reactive surface area and the rock to water ratio, i.e. the total reactive surface area per mass of water. It is well known that the estimation of the

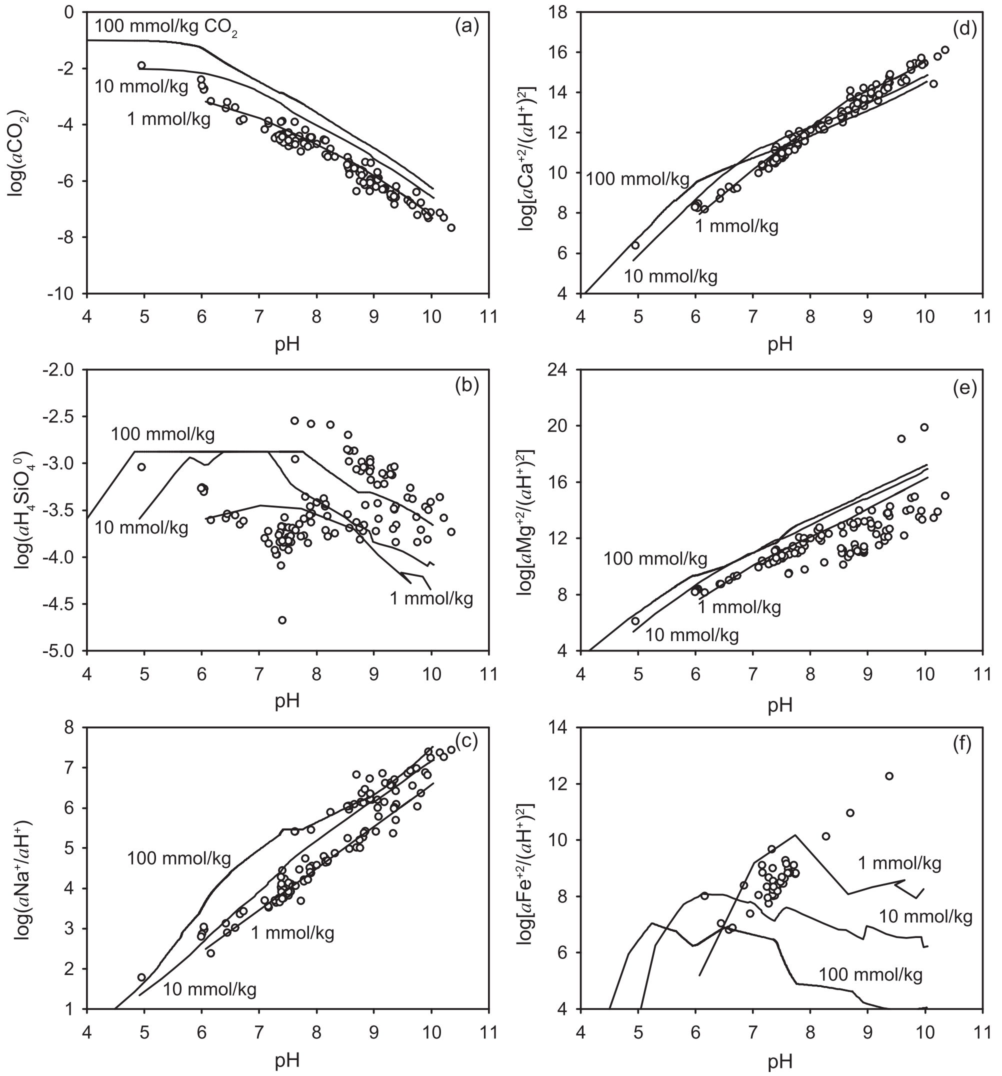

Fig. 11. pH plot of cation to proton activity ratios, CO_2 and $H_4SiO_4^0$ and comparison with natural data. The calculations were carried out at 25 °C using spring water (Vellankatla) with initial 1, 10 and 100 mmol/kg CO_2 and 100 g basaltic glass in 1 kg water.

true reactive surface area is difficult as well as the effects of surface roughness, porosity and secondary mineral coatings (e.g. White and Brantley, 2003). In the batch experiments of Gysi and Stefansson (2011), a well-characterized basaltic glass was used similar to the material to obtain the basaltic glass dissolution rates (Oelkers and Gíslason, 2001; Gíslason and Oelkers, 2003). The grain size used in the experiments ranged from 45 to 125 μm corresponding to geometric surface area of 250 cm^2/g. The measured BET surface area was 23,000 cm^2/g (Gíslason and Oelkers, 2003). The discrepancy between BET and geometric surface area is very large, and therefore we tried to vary the geometric surface area arbitrary between 50 and 250 cm^2/g to show that these small variations had some major effects on the simulated results depending on the timescale considered. For example, the time to reach a given pH and CO_2 concentration may vary by more than 100 days in our simplified system (Fig. 12). Such differences will further cumulate in simulations spanning longer times.

The basaltic dissolution rate used in the present study represents the Si steady-state basaltic glass dissolution rate normalized to the calculated geometric surface area at far-from-equilibrium conditions. However, when the solid approaches equilibrium saturation the dissolution rate will decrease. This effect is often quantified in terms of the chemical affinity of the dissolving phase (e.g. Lasaga, 1981; Helgeson et al., 1984; Murphy and Helgeson, 1987; Oelkers, 2001). Numerically, this requires knowledge of the equilibrium solubility constant for the basaltic glass. Number of studies have adopted this approach assuming the surface layer of the basaltic glass being represented by a Si-rich gel (Grambow, 1985; Berger et al., 1994) or a mixed hydrated gel containing $Si + Al \pm Fe,Ca,Mg$ (Bourcier et al., 1990; Daux et al., 1997; Oelkers and Gíslason, 2001; Gíslason and Oelkers, 2003; Marini, 2006). The approach used in the present study assumed the dissolution mechanism to progress into the formation of a Si–Al hydrated leached layer at the surface of the glass.

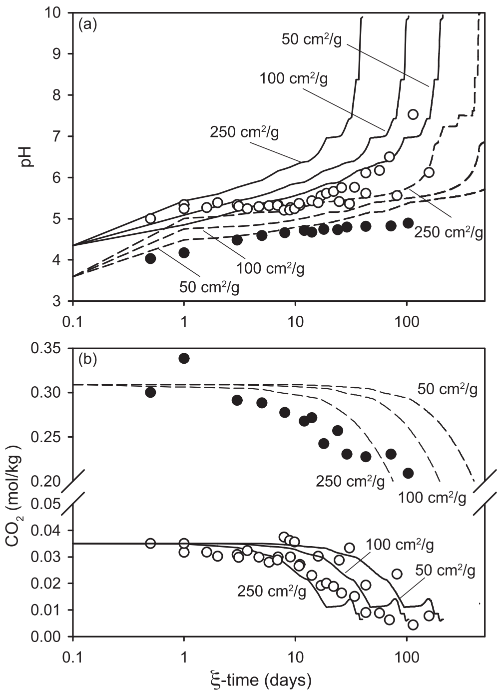

Fig. 12. pH (a) and dissolved CO_2 (b) versus ξ (reaction progress)-time and comparison with experimental data (Gysi and Stefansson, 2011). The calculations were carried out at 40 °C using spring water (Vellankatla) initially saturated with 1.2 and 13 bar CO_2 and 200 g basaltic glass in 1 kg water with variable reactive surface areas (50–250 cm^2/g). Black dots indicate experimental solutions at 13 bar pCO_2 and white dots indicate experiments <2 bar pCO_2.

The steady state dissolution rates are reached when the dissolution of the basaltic glass corresponds to the release and diffusion rates of other cations through the leached layers. The solubility of the basaltic glass is represented by the equilibrium solubility of the leached layer approximated to be equal to the sum of amorphous SiO_2 and $Al(OH)_3$. However, using the same convention but assuming impurities of other elements like Fe, Mg and Ca in the leached layer will change the basaltic glass equilibrium solubility and in turn affects the calculated chemical affinity on the dissolution rates. The model calculations showed relatively fast dissolution rates that were characterized by fast elemental release compared to experimental observations (Fig. 13). In the present model assumptions, the saturation state of the basaltic glass was strongly dependent on the Al and Si content in solution that in turn was buffered primarily by the formation of SiO_2 and Al–Si minerals, clays and zeolites. The calculated chemical affinity was then constant over time and therefore the choice of SiO_2 polymorph affected the calculated dissolution rates. Using the same simulation setup without allowing SiO_2 and Al–Si minerals to precipitate, the saturation state of the glass was controlled mainly by the formation of clay minerals. The chemical affinity was then not constant but decreased with time while the basaltic glass became closer and closer to saturation with reaction progress and eventually stopped to dissolve as it reached equilibrium. The effect of the secondary mineralogy chosen in the model was found to have a crucial role on the calculated dissolution rates, whereas the effect of including impurities in the leached layer such as for example Fe or Ti had only minor influence on the overall rate. These effects were tested by adding $Fe(OH)_3$ to the leached layer formula $SiAl_{0.35}Fe_{0.012}O_2(OH)_{1.086}$ with a calculated apparent Gibbs energy of $-1{,}263{,}401$ J mol^{-1} (25 °C). Therefore, the calculated dissolution rates were somewhat dependent on the chemical affinity that in turn depends on the approach to calculate basaltic glass equilibrium solubility, especially the Al–Si phases used to describe the leached layer.

In the model calculations, the basaltic glass was assumed to dissolve stoichiometrically. This is in agreement with experimental observations of water–basaltic glass batch experiments under low CO_2 conditions and neutral to alkaline pH values (Gíslason and Eugster, 1987a; Daux et al., 1994). On the other hand, Gysi and Stefánsson (2011) observed preferential release of Fe compared to Na whereas Ca, Mg and Na dissolved stoichiometrically during CO_2–water–basaltic glass interaction at pH <6.5. Modeling non-stoichiometric dissolution is difficult and requires basic modification of the dissolution rate formulas and mechanisms applied. Moreover, the cause of the non-stoichiometric elemental release is uncertain. It may be due to actual dissolution mechanism or mineral impurities in the basaltic glass.

4. CO_2 SEQUESTRATION INTO BASALTS

The results from the present study may be used to retrieve the optimal conditions for CO_2 sequestration into basalts at low temperatures. Physical aspects during CO_2 injection are of importance such as pore space and rock fractures, which are essential for the geochemical reactions to be optimized. However, this study focuses on the geochemical aspects during CO_2–water–basalt interaction. Different variables such as reactive surface area per unit of solution, acid supply, temperature and oxidation state of the starting solution can be adjusted in order to achieve the most ideal conditions for CO_2 mineralization.

Initially, at elevated CO_2 concentrations the pH of the system is buffered by CO_2 ionization, basaltic glass dissolution and secondary mineral formation with Fe(II), Ca and Mg carbonate mineral formation. Reduced conditions favor consequently the carbonate mineralization. The carbonate compositions may vary, with initially Fe–Mg carbonates ($Mg_{0.25}Fe_{0.75}CO_3$) followed by Ca–Mg–Fe carbonates ($Ca_{0.25}Mg_{0.25}Fe_{0.50}CO_3$) and the incorporation of more Mg and especially Ca with time and increasing temperature. Increased CO_2 concentrations shift the overall reaction path in time and the amount of dissolved basaltic glass needed to mineralize the CO_2 increases.

The mass fraction of clay mineral formation compared to carbonates decreases with increasing initial CO_2 content, whereas the amount of mineralized SiO_2 increases with increasing initial CO_2. The formation of SiO_2 lowers the availability of Si needed for clay precipitation. Therefore, increased initial CO_2 content may favor the formation of carbonates that compete with clay minerals upon reaction progress for the Ca, Mg and Fe ions. Since the time needed

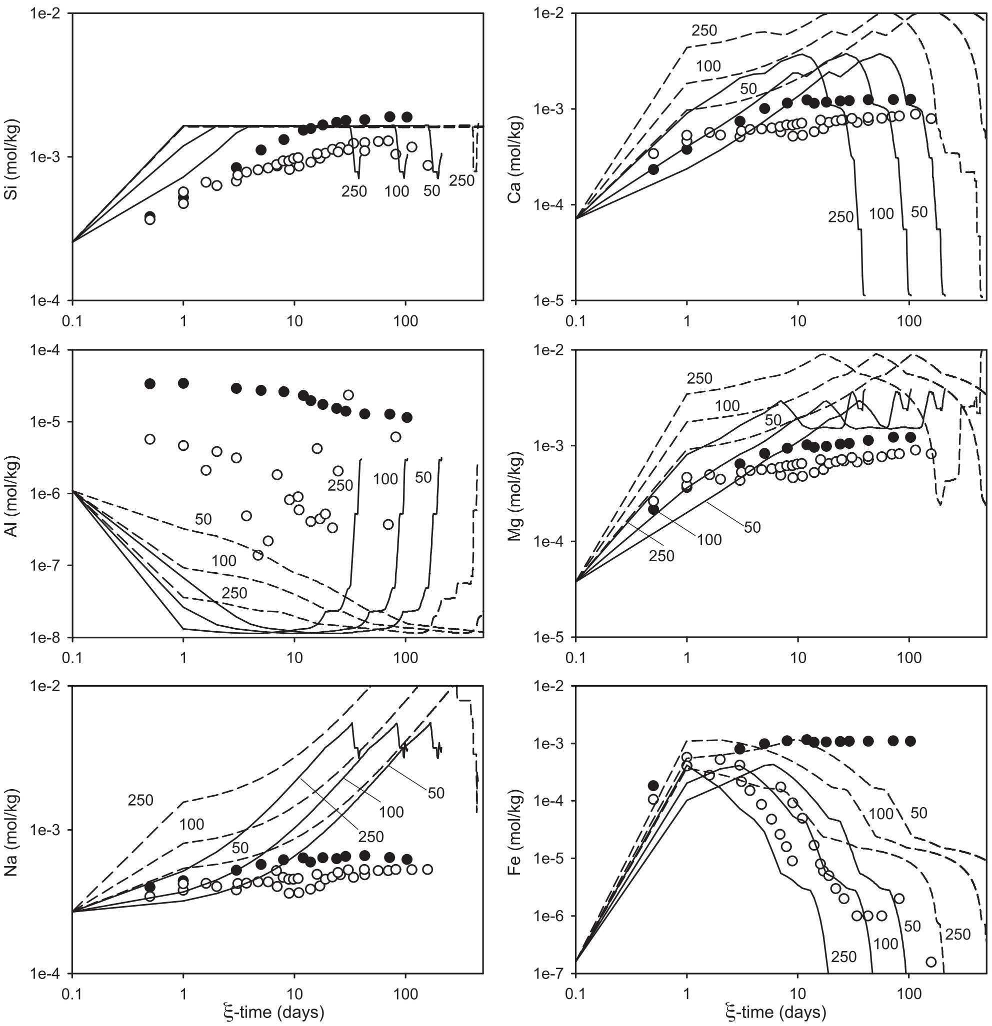

Fig. 13. Major cations versus ξ (reaction progress)-time and comparison with experimental data (Gysi and Stefánsson, 2011). The calculations were carried out at 40 °C using spring water (Vellankatla) initially saturated with 1.2 and 13 bar CO_2 and 200 g basaltic glass in 1 kg water with variable reactive surface areas (50–250 cm^2/g). Black dots indicate experimental solutions at 13 bar pCO_2 and white dots indicate experiments <2 bar pCO_2.

to reach the basalt alteration buffered step increases with increasing CO_2, the mass fluxes need to be increased in order to accelerate and optimize the CO_2 mineralization process at elevated CO_2 and not getting the system locked at the basaltic glass minimum dissolution rate. One way consists of increasing the rock to water ratio, namely the reactive surface area of the primary dissolving phase. In CO_2 sequestrations sites, this variable is fixed by the flow path of the water through the basalts as well as the rock porosity. Another way consists of increasing the temperature with injection depth due to the increasing geothermal gradient.

The chemical mass fluxes resulting from the basaltic glass dissolution and the secondary mineral precipitation can be written in simplified form in order to study the reaction stoichiometry as a function of reaction progress and initial CO_2 concentration. For systems initially saturated at 2 bar pCO_2 and containing 100 g basaltic glass with 1000 ml spring water (Vellankatla) the reaction stoichiometry was

$$\begin{aligned}&\text{basaltic glass} + H^+ + H_2O = 0.65SiO_2 + 0.31Ca_{0.25}Mg_{0.25}Fe_{0.50}CO_3\\&\quad + 0.15\ \text{allophane} + 0.04\text{Ca–(Mg)–Fe(III)–Fe(II)smectite}\end{aligned} \tag{7}$$

$$\begin{aligned}&\text{basaltic glass} + H^+ + H_2O = 0.21CaCO_3 + 0.19\text{Ca–Mg–Fe(II)smectite}\\&\quad + 0.12Mg_{0.75}Fe_{0.25}CO_3 + 0.04\ \text{analcime}\\&\quad + 0.03\text{Ca–(Mg)–Fe(III)–Fe(II)smectite} + 0.02\ \text{thomsonite}\end{aligned} \tag{8}$$

at pH 6 and 9, respectively. A similar reaction may be written for systems initially saturated at 30 bar pCO_2 and containing 400 g basaltic glass with 1000 ml spring water (Vellankatla) the reaction stoichiometry was

$$\begin{aligned}&\text{basaltic glass} + H^+ + H_2O = 0.71SiO_2 + 0.47Ca_{0.25}Mg_{0.50}Fe_{0.25}CO_3\\&\quad + 0.15\ \text{allophane} + 0.12CaCO_3 + 0.09Ca_{0.25}Mg_{0.25}Fe_{0.50}CO_3\\&\quad + 0.03\text{Ca–(Mg)–Fe(III)–Fe(II)smectite}\end{aligned} \tag{9}$$

$$\begin{aligned}&\text{basaltic glass} + H^+ + H_2O = 0.21CaCO_3 + 0.18\text{Ca–Mg–Fe(II)smectite}\\&\quad + 0.14Mg_{0.75}Fe_{0.25}CO_3 + 0.06\ \text{analcime}\\&\quad + 0.03\text{Ca–(Mg)–Fe(III)–Fe(II)smectite} + 0.01\ \text{thomsonite}\end{aligned} \tag{10}$$

at pH 6 and 9, respectively. The calculated reaction stoichiometries indicate that at low reaction progress and pH of 6, the quantity and compositions of secondary minerals formed at elevated CO_2 (30 bar) are somewhat different than at low initial CO_2 (2 bar) with amounts of SiO_2 and carbonates forming per mole dissolved basaltic glass being greater (~0.6 mol carbonates per mole dissolved basaltic glass) at elevated compared to low CO_2 concentration (0.3 mol carbonates per mole dissolved basaltic glass). However, at high reaction progress and alkaline pH of 9, the reaction stoichiometry reaches the basalt alteration buffered step as the CO_2 has been mostly mineralized. The moles of secondary minerals formed per mole dissolved basaltic glass are then similar at low and elevated initial CO_2 concentrations, both system reaching a partial equilibrium.

Based on these findings the optimum CO_2 sequestration conditions can be evaluated. The best conditions are met when the system mineralizes a relatively high quantity of CO_2 per moles dissolved basaltic glass. The most effective conditions are found when the solution pH is below 6.5 and the initial CO_2 concentration is high (>10 bar pCO_2). Under these conditions, the mass of clay formation competing for Fe, Mg and Ca is at minimum compared to carbonate formation and iron is in the ferrous oxidation state. However, under these pH conditions the basaltic glass dissolution rate is at minimum (Gíslason and Oelkers, 2003) and therefore higher temperatures are favorable to enhance dissolution rates and mass fluxes.

In order to mineralize the maximum amount of CO_2 in the same time frame, there are two most practical ways. Either the system needs to contain a very high amount of water at low temperature (25 °C) and low initial pCO_2 (~2 bar), or the system can contain lower amounts of water at high temperatures (40–90 °C) and higher initial pCO_2 (~30 bar). For example, in order to mineralize ~1 mol of CO_2 per liter water at initial 30 bar pCO_2 and 25 °C the simulations indicate that it takes about 10 years and requires ~3 mol of basalt. By increasing the reaction temperature to 40 °C, the time required to mineralize the CO_2 is reduced to around 3 years and at 90 °C, the time is only 30 days. In order to mineralize the same amount of CO_2 (~1 mol) from a solution initially containing ~2 bar pCO_2 only 2 years are required at 25 °C, however, around 10 times more water is needed.

In order to mineralize a tonne of CO_2 in 3 years at least 22,700 L water are needed and ~8 tonnes of basalt if the water was saturated initially with 30 bar pCO_2. This corresponds to a reactive surface area of at least 200,000 m^2 or 10,000 cylindrical shaped cracks of 0.01 m radius and ~320 m length without considering porosity that enhances the mineralization process. Other parameters that need to be considered are the porosity of the rock as a function of reaction progress due to the dissolution of the primary phase, increasing the primary porosity, and secondary mineral formation that may reduce the porosity over time. Assuming a geothermal gradient of 30 °C/1000 m and a surface temperature of 10 °C, the optimal injection depth is at least 500–1000 m to mineralize all the CO_2 within 5 years at or above about 40 °C.

5. SUMMARY AND CONCLUSIONS

The effects of adding CO_2 to the water–basalt system were investigated at 25–90 °C by reaction path modeling at 0–30 bar pCO_2 and the results compared with laboratory experiments and natural data in order to characterize the reaction stoichiometries, secondary mineralogy and changes in solution chemistry as a function of reaction progress and pH.

The addition of CO_2 changes the water–basalt reaction path considerably. The changes are reflected by the chemical mass fluxes, secondary minerals formed and their compositions as well as mineral reaction kinetics. At low reaction progress and pH <6.5 the predominant mineralogy consists of SiO_2, simple Al–Si minerals and Ca–Mg–Fe carbonate solid solutions. Iron was found to play a key role for quantitative CO_2 mineralization. Upon quantitative CO_2 mineralization the water pH rose to >8. Under those conditions, the secondary mineral assemblage consists of Ca–Mg–Fe clays, zeolites and calcite. The competing reaction between clays and carbonates for Ca, Mg and Fe ions controls the carbonates forming and their compositions at a given pH and as a function of reaction progress. Further, the oxidation state of Fe plays a crucial role for initial carbonate mineralization.

The CO_2–water–basalt simulations generated in the present study compared well with experimental and natural data. The reaction stoichiometries are reproduced fairly well, whereas discrepancies are mainly found in the element mass fluxes with time due to the dissolution kinetics of the primary phase, including problems associated to the reactive surface area and dissolution mechanisms. The simulations indicate that the secondary minerals forming and their compositions and quantity vary with pH. This pH dependence affects also the element mobility in solution. The comparison with natural and experimental data strongly suggest that the overall CO_2–water–basalt interaction is controlled by acid supply, cation release and proton consumption by the primary rock dissolution as well as the formation of secondary minerals.

In particular, the composition and quantity of carbonates forming is dependent on the initial acid supply, rock to water ratio (reactive surface area) and temperature. In order to sequestrate effectively CO_2 into basalts it is necessary to consider that even though the amount of CO_2 mineralizing per moles basaltic glass dissolved increases initially with increasing initial CO_2 content, the overall reaction path gets shifted to the CO_2–basalt alteration buffered system with increasing CO_2. It follows that the system needs more time as well as more dissolved basaltic glass to reach pH values >8. In order to optimize low temperature mineral carbonations, a fine balance between initial CO_2 (acid supply), rock to water ratio and temperature needs to be adjusted in order to mineralize effectively CO_2 on a reasonable time scale.

ACKNOWLEDGMENTS

This research was funded by the European Union through MIN-GRO Research and Training Network (Contract No. MRTN-CT-2006-035488) and by the Science Institute University of Iceland. The authors like to thank L. Marini and an anonymous reviewer for their useful comments on the manuscript.

APPENDIX A

Apparent standard Gibbs energy (J mol^{-1}) for selected aqueous species from 25 to 300 °C at water saturation pressures.[a]

t (°C)	25	50	75	100	125	150	175	200	225	250	275	300
p_{sat} (bar)	1.0	1.0	1.0	1.0	2.3	4.8	8.9	15.5	25.5	39.7	59.4	85.8
$H_4SiO_4^0$[b]	−1,309,266	−1,313,977	−1,319,135	−1,324,687	−1,330,589	−1,336,797	−1,343,273	−1,349,984	−1,356,896	−1,363,979	−1,371,205	−1,378,548
H_2O (l)	−237,183	−239,007	−240,977	−243,082	−245,316	−247,664	−250,124	−252,693	−255,354	−258,111	−260,960	−263,889
Mg^{2+}	−453,985	−450,521	−447,039	−443,550	−440,035	−436,475	−432,847	−429,128	−425,283	−421,253	−416,990	−412,509
K^+	−282,462	−284,997	−287,562	−290,156	−292,775	−295,416	−298,072	−300,742	−303,407	−306,068	−308,700	−311,290
Na^+	−261,881	−263,383	−264,981	−266,667	−268,437	−270,286	−272,198	−274,165	−276,169	−278,198	−280,223	−282,228
Ca^{2+}	−552,790	−551,351	−549,857	−548,309	−546,694	−544,995	−543,196	−541,280	−539,213	−536,954	−534,447	−531,682
Fe^{2+}	−91,504	−88,831	−86,115	−83,358	−80,550	−77,672	−74,701	−71,618	−68,387	−64,965	−61,291	−57,375
$Fe(OH)_4^-$[c]	−845,026	−847,030	−849,423	−852,256	−855,515	−859,180	−863,209	−867,552	−872,142	−876,891	−881,669	−886,284
$Al(OH)_4^-$[d]	−1,305,771	−1,308,538	−1,311,694	−1,315,183	−1,319,000	−1,322,994	−1,327,133	−1,331,212	−1,335,175	−1,338,725	−1,341,719	−1,343,889
H^+	0	0	0	0	0	0	0	0	0	0	0	0
HCO_3^-	−586,940	−589,371	−591,760	−594,107	−596,396	−598,613	−600,730	−602,714	−604,504	−606,019	−607,140	−607,672

[a] Unless otherwise indicated, data are from SUPCRT92 (Johnson et al., 1992), slop98.dat database.

[b] Solubility measurements from Gunnarsson and Arnórsson (2000) combined with quartz from Richet et al. (1982), amorphous silica from Robie et al. (1979) and liquid water from slop98.dat.

[c] Solubility measurements from Diakonov et al. (1999) combined with Fe_2O_3 from Hemingway (1990).

[d] Solubility measurements from Bénézeth et al. (2001) and Palmer et al. (2001), calculated from Gibbs free energy and enthalpy of boehmite from Verdes (1990) and Verdes et al. (1992), and heat capacity from Hemingway et al. (1991).

APPENDIX B

Apparent standard Gibbs energy (J mol^{-1}) for selected secondary minerals from 25 to 300 °C at water saturation pressures.[a]

Mineral	25 °C	50 °C	75 °C	100 °C	125 °C	150 °C	175 °C	200 °C	225 °C	250 °C	275 °C	300 °C
Carbonates												
Calcite	−1,128,810	−1,131,207	−1,133,771	−1,136,493	−1,139,364	−1,142,378	−1,145,528	−1,148,805	−1,152,202	−1,155,709	−1,159,319	−1,163,022
Siderite[b]	−682,800	−685,273	−687,911	−690,708	−693,655	−696,747	−699,976	−703,335	−706,818	−710,416	−714,123	−717,931
Magnesite	−1,027,740	−1,029,447	−1,031,308	−1,033,321	−1,035,476	−1,037,770	−1,040,196	−1,042,749	−1,045,422	−1,048,209	−1,051,102	−1,054,094
Ankerite	−1,819,290	−1,824,134	−1,829,309	−1,834,801	−1,840,590	−1,846,666	−1,853,014	−1,859,620	−1,866,468	−1,873,543	−1,880,829	−1,888,310
Dolomite	−2,161,510	−2,165,573	−2,169,955	−2,174,646	−2,179,627	−2,184,890	−2,190,420	−2,196,204	−2,202,228	−2,208,477	−2,214,936	−2,221,590
$Ca_{0.25}Mg_{0.50}Fe_{0.25}$ carbonate[c]	−969,350	−971,637	−974,084	−976,686	−979,434	−982,324	−985,348	−988,500	−991,772	−995,158	−998,650	−1,002,240
$Ca_{0.25}Mg_{0.25}Fe_{0.50}$ carbonate[c]	−883,115	−885,593	−888,235	−891,033	−893,979	−897,068	−900,293	−903,646	−907,121	−910,710	−914,405	−918,199
$Mg_{0.25}Fe_{0.75}$ carbonate[c]	−770,429	−772,827	−775,388	−778,106	−780,972	−783,981	−787,126	−790,401	−793,798	−797,310	−800,931	−804,651

$Mg_{0.50}Fe_{0.50}$ carbonate[c]	−856,988	−859,222	−861,616	−864,165	−866,860	−869,697	−872,669	−875,769	−878,991	−882,327	−885,771	−889,315
$Mg_{0.75}Fe_{0.25}$ carbonate[c]	−942,899	−944,914	−947,087	−949,412	−951,882	−954,492	−957,236	−960,108	−963,100	−966,206	−969,420	−972,733
Silica polymorphs												
Quartz[d]	−856,281	−857,366	−858,544	−859,809	−861,157	−862,582	−864,082	−865,653	−867,292	−868,997	−870,764	−872,594
Amorphous silica[d]	−850,559	−851,789	−853,106	−854,506	−855,983	−857,536	−859,159	−860,852	−862,612	−864,437	−866,325	−868,275
Moganite[e]	−851,313	−852,814	−854,405	−856,083	−857,815	−859,603	−861,431	−863,280	−865,127	−866,947	−868,714	−870,394
Chalcedony	–	–	–	–	–	–	–	–	–	–	–	–
Zeolites												
Analcime[f]	−3,082,900	−3,088,958	−3,095,438	−3,102,318	−3,109,570	−3,117,181	−3,125,132	−3,133,406	−3,141,985	−3,150,851	−3,159,986	−3,169,371
Chabazite–Ca[g]	−7,154,665	−7,169,952	−7,186,598	−7,204,585	−7,223,858	−7,244,394	−7,266,155	−7,289,095	−7,313,169	−7,338,327	−7,364,520	−7,391,694
Thomsonite[g]	−11,469,875	−11,489,550	−11,510,716	−11,533,326	−11,557,285	−11,582,546	−11,609,039	−11,636,689	−11,665,422	−11,695,159	−11,725,822	−11,757,328
Heulandite-Ca[g]	−9,723,993	−9,743,104	−9,763,782	−9,785,976	−9,809,596	−9,834,598	−9,860,920	−9,888,494	−9,917,254	−9,947,131	−9,978,054	−10,009,950
Stilbite-Ca[g]	−9,962,230	−9,983,177	−10,005,719	−10,029,799	−10,055,315	−10,082,217	−10,110,433	−10,139,888	−10,170,506	−10,202,210	−10,234,922	−10,268,561
Scolecite[g]	−5,598,146	−5,607,730	−5,618,096	−5,629,226	−5,641,080	−5,653,647	−5,666,903	−5,680,825	−5,695,387	−5,710,562	−5,726,322	−5,742,638
Natrolite[g]	−5,317,040	−5,326,406	−5,336,501	−5,347,301	−5,358,761	−5,370,863	−5,383,578	−5,396,873	−5,410,718	−5,425,080	−5,439,924	−5,455,216
Mesolite[g]	−5,504,512	−5,514,024	−5,524,300	−5,535,320	−5,547,042	−5,559,454	−5,572,530	−5,586,243	−5,600,565	−5,615,469	−5,630,923	−5,646,896
Mordenite-Ca[g]	−6,401,646	−6,414,901	−6,429,177	−6,444,425	−6,460,574	−6,477,589	−6,495,417	−6,514,009	−6,533,316	−6,553,285	−6,573,867	−6,595,009
Phyllosilicates												
Ca-Beidellite[c]	−5,364,146	−5,369,098	−5,375,030	−5,381,828	−5,389,391	−5,397,655	−5,406,562	−5,416,058	−5,426,097	−5,436,634	−5,447,627	−5,459,035
Mg-Beidellite[c]	−5,357,501	−5,362,239	−5,367,754	−5,373,948	−5,380,730	−5,388,048	−5,395,853	−5,404,100	−5,412,749	−5,421,763	−5,431,106	−5,440,744
Ca-nontronite[c]	−4,495,291	−4,501,534	−4,508,461	−4,516,006	−4,524,098	−4,532,700	−4,541,773	−4,551,279	−4,561,183	−4,571,452	−4,582,052	−4,592,950
Mg-nontronite[c]	−4,488,646	−4,494,783	−4,501,608	−4,509,054	−4,517,049	−4,525,556	−4,534,534	−4,543,947	−4,553,758	−4,563,934	−4,574,442	−4,585,248
Ca-saponite[c]	−5,624,278	−5,630,249	−5,637,009	−5,644,470	−5,652,547	−5,661,191	−5,670,355	−5,679,993	−5,690,066	−5,700,535	−5,711,362	−5,722,511
Mg-saponite[c]	−5,616,295	−5,622,158	−5,628,814	−5,636,173	−5,644,151	−5,652,698	−5,661,764	−5,671,306	−5,681,283	−5,691,656	−5,702,388	−5,713,442
Ca–(Mg)–Fe smectite[c]	−5,127,692	−5,133,100	−5,139,263	−5,146,092	−5,153,502	−5,161,447	−5,169,879	−5,178,756	−5,188,039	−5,197,692	−5,207,681	−5,217,969
Mg-clay natural[c]	−5,554,394	−5,560,033	−5,566,458	−5,573,579	−5,581,313	−5,589,611	−5,598,423	−5,607,709	−5,617,426	−5,627,539	−5,638,010	−5,648,805
Ca–Fe clay natural[c]	−4,690,204	−4,696,693	−4,703,881	−4,711,703	−4,720,089	−4,729,001	−4,738,399	−4,748,246	−4,758,506	−4,769,145	−4,780,129	−4,791,424
Ca–Mg–Fe clay 1[c]	−5,195,945	−5,201,621	−5,208,074	−5,215,210	−5,222,946	−5,231,232	−5,240,020	−5,249,266	−5,258,933	−5,268,982	−5,279,378	−5,290,085
Ca–Mg–Fe clay 2[c]	−5,441,914	−5,448,108	−5,455,094	−5,462,787	−5,471,104	−5,479,997	−5,489,418	−5,499,324	−5,509,676	−5,520,436	−5,531,568	−5,543,036
Ca–Mg–Fe clay 3[c]	−5,165,925	−5,172,788	−5,180,454	−5,188,839	−5,197,861	−5,207,475	−5,217,631	−5,228,288	−5,239,406	−5,250,948	−5,262,876	−5,275,155
Ca–Mg–Fe clay 4[c]	−5,178,181	−5,184,899	−5,192,415	−5,200,644	−5,209,506	−5,218,953	−5,228,939	−5,239,421	−5,250,359	−5,261,716	−5,273,455	−5,285,542
Celadonite natural[c]	−5,142,104	−5,148,734	−5,156,156	−5,164,281	−5,173,023	−5,182,335	−5,192,169	−5,202,480	−5,213,230	−5,224,382	−5,235,898	−5,247,744
Celadonite-Fe	−5,127,780	−5,136,074	−5,145,045	−5,154,670	−5,164,912	−5,175,753	−5,187,163	−5,199,114	−5,211,575	−5,224,513	−5,237,897	−5,251,693
Chlorite	−8,078,470	−8,089,214	−8,101,033	−8,113,902	−8,127,768	−8,142,604	−8,158,369	−8,175,018	−8,192,504	−8,210,778	−8,229,789	−8,249,485
Hydrated Al–silicates												
Kaolinite	−3,801,720	−3,807,046	−3,812,829	−3,819,055	−3,825,695	−3,832,736	−3,840,156	−3,847,933	−3,856,044	−3,864,468	−3,873,178	−3,882,152
Imogolite (natural gel)[h]	−2,927,497	−2,932,986	−2,938,999	−2,945,491	−2,952,409	−2,959,725	–	–	–	–	–	–
Allophane Al/Si 2.02[h]	−3,066,319	−3,071,914	−3,078,109	−3,084,855	−3,092,096	−3,099,794	–	–	–	–	–	–
Allophane Al/Si 1.64[h]	−3,233,617	−3,239,999	−3,247,012	−3,254,598	−3,262,697	−3,271,267	–	–	–	–	–	–
Allophane Al/Si 1.26[h]	−3,551,795	−3,557,962	−3,564,816	−3,572,291	−3,580,310	−3,588,832	–	–	–	–	–	–
Leached BG layer[i]	−1,254,899	−1,256,505	−1,258,404	−1,260,566	–	–	–	–	–	–	–	–

(*continued on next page*)

Appendix B (*continued*)

Mineral	25 °C	50 °C	75 °C	100 °C	125 °C	150 °C	175 °C	200 °C	225 °C	250 °C	275 °C	300 °C
Al- and Fe-oxyhydroxides												
Gibbsite[j]	−1,155,257	−1,156,331	−1,157,994	−1,160,171	–	–	–	–	–	–	–	–
Goethite	−490,860	−492,447	−494,184	−496,064	−498,078	−500,223	−502,490	−504,874	−507,369	−509,968	−512,665	−515,453
Ferrihydrite (2-line)[k]	−708,500	−711,632	−714,914	−718,339	−721,898	−725,588	−729,400	−733,329	−737,369	−741,513	−745,755	−750,088

[a] Unless otherwise indicated, data are calculated from the Holland and Powell (1998) database.

[b] Robie and Hemingway (1995).

[c] This study (see text).

[d] Gunnarsson and Arnórsson (2000) with standard state properties of quartz and amorphous silica from Richet et al. (1982) and Robie et al. (1979), respectively.

[e] Gíslason et al. (1997), quartz from Richet et al. (1982), heat capacity coefficients from Holland and Powell (1998), *V*° from XRD data from Heaney and Post (2001).

[f] Neuhoff et al. (2004) from analcime data from Johnson et al. (1982).

[g] Calculated from database in Neuhoff (2000).

[h] Su and Harsh (1994, 1998) using boehmite from Verdes (1990), Verdes et al. (1992) and Hemingway et al. (1991), and H_2O(l) and H_4SiO_4 from Appendix A.

[i] Hydrated basaltic glass, thermodynamic properties retrieved by summation of Gibbsite and amorphous SiO_2.

[j] Calculated and extrapolated to 100 °C from Verdes et al. (1992) using OH^- from slop98.dat (SUPCRT92, Johnson et al., 1992) and $Al(OH)_4^-$ from Appendix A.

[k] Majzlan et al. (2004), heat capacity coefficients and *V*° assumed to be equal to goethite from Holland and Powell (1998).

REFERENCES

Allen M. R., Framer D. J., Huntingford C., Jones C. D., Lowe J. A., Meinshausen M. and Meinshausen N. (2009) Warming caused by cumulative carbon emissions towards the trillionth tonne. *Nature* **458**, 1163–1166.

Arnórsson S., Sigurdsson S. and Svavarsson H. (1982) The chemistry of geothermal waters in Iceland: I. Calculation of aqueous speciation from 0 to 370 °C. *Geochim. Cosmochim. Acta* **46**, 1513–1532.

Bénézeth P., Palmer D. A. and Wesolowski D. J. (2001) Aqueous high-temperature solubility studies. II. The solubility of boehmite at 0.03 m ionic strength as a function of temperature and pH as determined by in situ measurements. *Geochim. Cosmochim. Acta* **65**, 2097–2111.

Berger G., Claparols C., Guy C. and Daux V. (1994) Dissolution rate of a basalt glass in silica-rich solutions: implications for long-term alteration. *Geochim. Cosmochim. Acta* **58**, 4875–4886.

Berman R. G. and Brown T. H. (1985) Heat capacity of minerals in the system Na_2O–K_2O–CaO–MgO–FeO–Fe_2O_3–Al_2O_3–SiO_2–TiO_2–H_2O–CO_2: representation, estimation, and high temperature extrapolation. *Contrib. Mineral. Petrol.* **89**, 168–183.

Berner E. K. and Berner R. A. (1995) *Global Environment: Water, Air and Geochemical Cycles*. Prentice Hall, p. 376.

Bourcier W. L., Peiffer D. W., Knauss K. G., McKeegan K. D. and Smith D. K. (1990) A kinetic model for borosilicate glass dissolution based on the dissolution affinity of a surface alteration layer. *Mater. Res. Soc. Symp. Proc.* **176**, 209–216.

Chermak J. A. and Rimstidt J. D. (1989) Estimating the thermodynamic properties ($\Delta G_f°$ and $\Delta H_f°$) of silicate minerals at 298K from the sum of polyhedral contributions. *Am. Mineral.* **74**, 1023–1031.

Crovisier J. L., Honnorez J., Fritz B. and Petit J. C. (1992) Dissolution of subglacial volcanic glasses from Iceland: laboratory study and modelling. *Appl. Geochem.* **1**, 55–81.

Crovisier J. L., Advocat T. and Dussossoy J.-L. (2003) Nature and role of natural alteration gels formed on the surface of ancient volcanic glasses (natural analogs of waste containment glasses). *J. Nucl. Mater.* **321**, 91–109.

Daux V., Crovisier J. L., Hemond C. and Petit J. C. (1994) Geochemical evolution of basaltic rocks subjected to weathering: fate of the major elements, rare earth elements, and thorium. *Geochim. Cosmochim. Acta* **58**, 4941–4954.

Daux V., Guy C., Advocat T., Crovisier J. L. and Stille P. (1997) Kinetic aspects of basaltic glass dissolution at 90 °C: role of aqueous silicon and aluminium. *Chem. Geol.* **142**, 109–126.

Denbigh K. (1971) *The Principles of Chemical Equilibrium*, third ed. Cambridge University Press, p. 494.

Dessert C., Dupré B., Gaillardet J., François L. M. and Allègre C. J. (2003) Basalt weathering laws and the impact of basalt weathering on the global carbon cycle. *Chem. Geol.* **202**, 257–273.

Diakonov I. I., Schott J., Martin F., Harrichourry J.-C. and Escalier J. (1999) Iron(III) solubility and speciation in aqueous solutions. Experimental study and modelling: part 1. Hematite solubility from 60 to 300 °C in NaOH–NaCl solutions and thermodynamic properties of $Fe(OH)_4^-$(aq). *Geochim. Cosmochim. Acta* **63**, 2247–2261.

Eggleton R. A. and Keller J. (1982) The palagonitization of limburgite glass – a TEM study. *Neues Jahrb. Mineral.* **7**, 321–336.

Fritz B., Clément A., Amal Y. and Noguera C. (2009) Simulation of the nucleation and growth of simple clay minerals in weathering processes: the NANOKIN code. *Geochim. Cosmochim. Acta* **73**, 1340–1358.

Furnes H. (1975) Experimental plagonitization of basaltic glasses of varied composition. *Contrib. Mineral. Petrol.* **50**, 103–113.

Furnes H. (1984) Chemical changes during progressive subaerial palagonitization of subglacial olivine tholeiite hyaloclastite: a microprobe study. *Chem. Geol.* **43**, 271–285.

Gaillardet J., Dupré B., Louvat P. and Allègre C. J. (1999) Global silicate weathering and CO_2 consumption rates deduced from the chemistry of large rivers. *Chem. Geol.* **159**, 3–30.

Garcia B., Beaumont V., Perfetti E., Rouchon V., Blanchet D., Oger P., Dromart G., Huc A. Y. and Haeseler F. (2010) Experiments and geochemical modelling of CO_2 sequestration by olivine: potential, quantification. *Appl. Geochem.* **25**, 1383–1396.

Garrels R. M. (1967) Genesis of some ground waters from igneous rocks. In *Researches in Geochemistry*, vol. 2 (ed. P. H. Abelson). Wiley, New York., pp. 405–420.

Ghiara M. R. and Petti C. (1996) Chemical alteration of volcanic glasses and related control by secondary minerals: experimental studies. *Aquat. Geochem.* **1**, 329–354.

Ghiara M. R., Franco E., Petti C., Stanzione D. and Valentino G. M. (1993) Hydrothermal interaction between basaltic glass, deionized water and seawater. *Chem. Geol.* **104**, 125–138.

Gíslason S. R. and Eugster H. P. (1987a) Meteoric water–basalt interactions. I: a laboratory study. *Geochim. Cosmochim. Acta* **51**, 2827–2840.

Gíslason S. R. and Eugster H. P. (1987b) Meteoric water–basalt interactions. II: a field study in N.E. Iceland. *Geochim. Cosmochim. Acta* **51**, 2841–2855.

Gíslason S. R. and Oelkers E. H. (2003) Mechanism, rates, and consequences of basaltic glass dissolution: II. An experimental study of the dissolution rates of basaltic glass as a function of pH and temperature. *Geochim. Cosmochim. Acta* **67**, 3817–3832.

Gíslason S. R., Veblen D. R. and Livi K. J. T. (1993) Experimental meteoric water–basalt interactions: characterization and interpretation of alteration products. *Geochim. Cosmochim. Acta* **57**, 1459–1471.

Gíslason S. R., Arnórsson S. and Ármannsson H. (1996) Chemical weathering of basalt in SW Iceland: effects of runoff, age of rocks and vegetative/glacial cover. *Am. J. Sci.* **296**, 837–907.

Gíslason S. R., Heaney P. J., Oelkers E. H. and Schott J. (1997) Kinetic and thermodynamic properties of moganite, a novel silica polymorph. *Geochim. Cosmochim. Acta* **61**, 1193–1204.

Gíslason S. R., Wolff-Boenisch D., Stefánsson A., Oelkers E. H., Gunnlaugsson E., Sigurdardottir H., Sigfússon B., Broecker W. S., Matter J. M., Stute M., Axelsson G. and Fridriksson Th. (2010) Mineral sequestration of carbon dioxide in basalt: a pre-injection overview of the CarbFix project. *Int. J. Greenhouse Gas Control* **4**, 537–545.

Goldberg D. S., Takahashi T. and Slagle A. L. (2008) Carbon dioxide sequestration in deep-sea basalts. *Proc. Natl. Acad. Sci. USA* **105**, 9920–9925.

Grambow B. (1985) A general rate equation for nuclear waste glass corrosion. *Mater. Res. Soc. Symp. Proc.* **44**, 15–27.

Gunnarsson I. and Arnórsson S. (2000) Amorphous silica solubility and the thermodynamic properties of H_4SiO_4 in the range of 0 to 350 °C at P_{sat}. *Geochim. Cosmochim. Acta* **64**, 2295–2307.

Gysi A. P. and Stefánsson A. (2008) Numerical modelling of CO_2–water–basalt interaction. *Mineral. Mag.* **72**, 55–59.

Gysi A. P. and Stefánsson A. (2011) The interaction of CO_2-rich waters with basaltic glass - an experimental study at 40–250 °C and pCO_2 1–30 bar. Univ. Iceland Science Institute Report, RH-11-2011, pp. 45.

Hänchen M., Prigiobbe V., Baciocchi R. and Mazzotti M. (2008) Precipitation in the Mg-carbonate system – effects of temperature and CO_2 pressure. *Chem. Eng. Sci.* **63**, 1012–1028.

Heaney P. J. and Post J. E. (2001) Evidence for I2/a to Imab phase transition in the silica polymorph moganite at 570K. *Am. Mineral.* **86**, 1358–1366.

Helgeson H. C. (1968) Evaluation of irreversible reactions in geochemical processes involving minerals and aqueous solutions – I. Thermodynamic relations. *Geochim. Cosmochim. Acta* **32**, 853–877.

Helgeson H. C., Garrels R. M. and Mackenzie F. T. (1969) Evaluation of irreversible reactions in geochemical processes involving minerals and aqueous solutions – II. Applications. *Geochim. Cosmochim. Acta* **33**, 455–481.

Helgeson H. C., Kirkham D. H. and Flowers G. C. (1981) Theoretical prediction of the thermodynamic behavior of aqueous electrolytes at high pressures and temperatures; IV. Calculation of activity coefficients, osmotic coefficients, and apparent molal and standard and relative partial molal properties to 600 °C and 5 kb. *Am. J. Sci.* **281**, 1249–1516.

Helgeson H. C., Murphy W. M. and Aagaard P. (1984) Thermodynamic and kinetic constrains on reaction rates among minerals and aqueous solutions: II. Rate constants, effective surface area, and the hydrolysis of feldspars. *Geochim. Cosmochim. Acta* **48**, 2405–2432.

Hemingway B. S. (1990) Thermodynamic properties for bunsenite, NiO, magnetite, Fe_3O_4, and hematite, Fe_2O_3, with comments on selected oxygen buffer reactions. *Am. Mineral.* **75**, 781–790.

Hemingway B. S., Robie R. A. and Apps J. A. (1991) Revised values for the thermodynamic properties of boehmite, AlO(OH), and related species and phases in the system Al–H–O. *Am. Mineral.* **76**, 445–457.

Hill P. G. (1990) A unified fundamental equation for the thermodynamic properties of H_2O. *J. Phys. Chem. Ref. Data* **19**, 1233–1274.

Holland T. J. B. (1989) Dependence of entropy on volume for silicate and oxide minerals: a review and a predictive model. *Am. Mineral.* **74**, 5–13.

Holland T. J. B. and Powell R. (1998) An internally consistent thermodynamic data set for phases of petrological interest. *J. Metamorph. Geol.* **16**, 309–343.

Jercinovic M. J., Keil K., Smith M. R. and Schmitt R. A. (1990) Alteration of basaltic glasses from north-central British Columbia, Canada. *Geochim. Cosmochim. Acta* **54**, 2679–2696.

Johnson G. K., Flotow H. E., O'hare P. A. G. and Wise W. S. (1982) Thermodynamic studies of zeolites; analcime and dehydrated analcime. *Am. Mineral.* **67**, 736–748.

Johnson J. W., Oelkers E. H. and Helgeson H. C. (1992) SUPCRT92: a software package for calculating the standard molal thermodynamic properties of minerals, gases, aqueous species, and reactions from 1 to 5000 bar and 0 °C to 1000 °C. *Comput. Geosci.* **18**, 899–947.

Kelemen P. and Matter J. M. (2008) In situ carbonation of peridotite for CO_2 storage. *Proc. Natl. Acad. Sci. USA* **105**, 17295–17300.

Larsen O. and Postma D. (2001) Kinetics of reductive bulk dissolution of lepidocrocite, ferrihydrite, and goethite. *Geochim. Cosmochim. Acta* **65**, 1367–1379.

Lasaga A. C. (1981) Transition state theory. *Rev. Mineral.* **8**, 135–169.

Majzlan J., Navrotsky A. and Schwertmann U. (2004) Thermodynamics of iron oxides: part III. Enthalpies of formation and stability of ferrihydrite ($Fe(OH)_3$), schwertmannite ($FeO(OH)_{3/4}(SO4)_{1/8}$), and ε-Fe_2O_3. *Geochim. Cosmochim. Acta* **68**, 1049–1059.

Marini L. (2006) *Geological sequestration of carbon dioxide – thermodynamics kinetics and reaction path modeling*. Elsevier, Amsterdam, p. 453.

Marini L., Zuccolini M. V. and Saldi G. (2003) The bimodal pH distribution of volcanic lake waters. *J. Volcanol. Geotherm. Res.* **121**, 83–98.

Matter J. M., Broecker W. S., Stute M., Gíslason S. R., Oelkers E. H., Stefánsson A., Wolff-Boenisch D., Gunnlaugsson E., Axelsson G. and Björnsson G. (2009) Permanent carbon dioxide storage into basalt: the CarbFix pilot project, Iceland. *Energy Procedia* **1**, 3641–3646.

McGrail B. P., Schaef H. T., Ho A. M., Chien Y.-J., Dooley J. J. and Davidson C. L. (2006) Potential for carbon dioxide sequestration in flood basalts. *J. Geophys. Res.* **111**, B12201.

Murphy W. M. and Helgeson H. C. (1987) Thermodynamic and kinetic constrains on reaction rates among minerals and aqueous solutions. III. Activated complexes and the pH-dependence of the rates of feldspar, pyroxene, wollastonite and olivine hydrolysis. *Geochim. Cosmochim. Acta* **51**, 3137–3153.

Nesbitt H. W. and Wilson R. E. (1992) Recent chemical weathering of basalts. *Am. J. Sci.* **292**, 740–777.

Neuhoff P. S. (2000) Thermodynamic properties and parageneses of rock-forming zeolites. Ph.D. Thesis, Stanford University.

Neuhoff P. S., Fridriksson T., Arnórsson S. and Bird D. K. (1999) Porosity evolution and mineral paragenesis during low-grade metamorphism of basaltic lavas at Teigarhorn, eastern Iceland. *Am. J. Sci.* **299**, 467–501.

Neuhoff P. S., Hovis G. L., Balassone G. and Stebbins J. F. (2004) Thermodynamic properties of analcime solid solutions. *Am. J. Sci.* **304**, 21–66.

Neuhoff P. S., Rogers K. L., Stannius L. S., Bird D. K. and Pedersen A. K. (2006) Regional very low-grade metamorphism of basaltic lavas, Disko-Nuussuaq region, West Greenland. *Lithos* **92**, 33–54.

Oelkers E. H. (2001) A general kinetic description of multi-oxide silicate mineral and glass dissolution. *Geochim. Cosmochim. Acta* **65**, 3703–3719.

Oelkers E. H. and Gíslason S. R. (2001) The mechanism, rates and consequences of basaltic glass dissolution: I. An experimental study of the dissolution rates of basaltic glass as a function of aqueous Al, Si and oxalic acid concentration at 25 °C and pH = 3 and 11. *Geochim. Cosmochim. Acta* **65**, 3671–3681.

Oelkers E. H., Gíslason S. R. and Matter J. (2008) Mineral carbonation of CO_2. *Elements* **4**, 331–335.

Palmer D. A., Bénézeth P. and Wesolowski D. J. (2001) Aqueous high-temperature solubility studies. I. The solubility of boehmite as functions of ionic strength (to 5 molal, NaCl), temperature (100–290 °C), and pH as determined by in situ measurements. *Geochim. Cosmochim. Acta* **65**, 2081–2095.

Parkhurst D. L. and Appelo C. A. J. (1999) *User's guide to PHREEQC (Version2) – a computer program for speciation, batch-reaction, one-dimensional transport, and inverse geochemical calculations.* US Geological Survey Water-resources Investigation Report 99-4259, p. 312.

Pogge von Strandmann P. A. E., Burton K. W., James R. H., Van Calsteren P., Gislason S. R. and Sigfússon B. (2008) The influence of weathering processes on riverine magnesium isotopes in a basaltic terrain. *Earth Planet. Sci. Lett.* **276**, 187–197.

Richet P., Bottinga Y., Denielou L., Petitet J. P. and Tequi C. (1982) Thermodynamic properties of quartz, cristobalite and amorphous SiO_2: drop calorimetry measurements between 1000 and 1800K and a review from 0 to 2000K. *Geochim. Cosmochim. Acta* **46**, 2639–2658.

Robie R. A. and Hemingway B. S. (1995) Thermodynamic properties of minerals and related substances at 298.15K and 1 bar (10^5 Pascals) pressure and at higher temperatures. *US Geological Survey Bulletin* **2131**, p. 461.

Robie R. A., Hemingway B. S. and Fisher J. R. (1979) Thermodynamic properties of minerals and related substances at 298.15K and 1 bar (10^5 Pascals) pressure and at higher temperatures. *US Geological Survey Bulletin* **1452**, p. 456.

Rogers K. L., Neuhoff P. S., Pedersen A. K. and Bird D. K. (2006) CO_2 metasomatism in a basalt-hosted petroleum reservoir, Nuussuaq, West Greenland. *Lithos* **92**, 55–82.

Romanek C. S., Jiménez-López C., Navarro A. R., Sánchez-Román M., Sahai N. and Coleman M. (2009) Inorganic synthesis of Fe–Ca–Mg carbonates at low temperature. *Geochim. Cosmochim. Acta* **73**, 5361–5376.

Saldi D., Jordan G., Schott J. and Oelkers E. H. (2009) Magnesite growth rates as a function of temperature and saturation state. *Geochim. Cosmochim. Acta* **73**, 5646–5657.

Schaef H. T., McGrail B. P. and Owen A. T. (2010) Carbonate mineralization of volcanic province basalts. *Int. J. Greenhouse Gas Control* **4**, 249–261.

Shock E. L. and Helgeson H. C. (1988) Calculation of the thermodynamic and transport properties of aqueous species at high pressures and temperatures: correlation algorithms for ionic species and equation of state predictions to 5 kb and 1000 °C. *Geochim. Cosmochim. Acta* **52**, 2009–3036.

Shock E. L., Oelkers E. H., Johnson J. W., Sverjensky D. A. and Helgeson H. C. (1992) Calculations of the thermodynamic properties of aqueous species at high pressures and temperatures. Effective electrostatic radii, dissociation constants and standard partial molal properties to 1000 °C and 5 kbar. *J. Chem. Soc. Faraday Trans.* **88**, 803–826.

Singer A. (1974) Mineralogy of palagonitic material from material from the Golan Heights, Israel. *Clays Clay Miner.* **22**, 231–240.

Staudigel H. and Hart R. (1983) Alteration of basaltic glass: mechanisms and significance for the oceanic crust-seawater budget. *Geochim. Cosmochim. Acta* **47**, 337–350.

Stefánsson A. (2001) Dissolution of primary minerals in natural waters I. Calculations of mineral solubilities from 0 to 350 °C. *Chem. Geol.* **172**, 225–250.

Stefánsson A. and Arnórsson S. (2000) Feldspar saturation state in natural waters. *Geochim. Cosmochim. Acta* **64**, 2567–2584.

Stefánsson A. and Gíslason S. R. (2001) Chemical weathering of basalts, SW Iceland. Effect of rock crystallinity and secondary minerals on chemical fluxes to the ocean. *Am. J. Sci.* **301**, 513–556.

Stefánsson A., Gíslason S. R. and Arnórsson S. (2001) Dissolution of primary minerals in natural waters II. Mineral saturation state. *Chem. Geol.* **172**, 251–276.

Stroncik N. A. and Schmincke H.-U. (2001) The evolution of palagonite crystallisation, chemical changes and element budget. *Geochem. Geophys. Geosyst.* **2**, 1017.

Su C. and Harsh J. B. (1994) Gibbs free energies of formation at 298K for imogolite and gibbsite from solubility measurements. *Geochim. Cosmochim. Acta* **58**, 1667–1677.

Su C. and Harsh J. B. (1998) Dissolution of allophane as a thermodynamically unstable solid in the presence of boehmite at elevated temperatures and equilibrium vapor pressures. *Soil Sci.* **163**, 299–312.

Tanger J. C. and Helgeson H. C. (1988) Calculation of the thermodynamic and transport properties of aqueous species at high pressures and temperatures; revised equations of state for the standard partial molal properties of ions and electrolytes. *Am. J. Sci.* **288**, 19–98.

Tardy Y. and Fritz B. (1981) An ideal solid solution model for calculating solubility of clay minerals. *Clay Miner.* **16**, 361–373.

Tardy Y. and Garrels R. M. (1974) A method of estimating the Gibbs energies of formation of layer silicates. *Geochim. Cosmochim. Acta* **38**, 1101–1116.

Tardy Y. and Garrels R. M. (1976) Prediction of Gibbs energies of formation-I. Relationships among Gibbs energies of formation of hydroxides, oxides and aqueous ions. *Geochim. Cosmochim. Acta* **40**, 1051–1056.

Tardy Y. and Garrels R. M. (1977) Prediction of Gibbs energies of formation-II. Monovalent and divalent metal silicates. *Geochim. Cosmochim. Acta* **41**, 87–92.

Thorseth I. H., Furnes H. and Tumyr O. (1991) A textural and chemical study of Icelandic palagonite of varied composition and its bearing on the mechanism of the glass-palagonite transformation. *Geochim. Cosmochim. Acta* **55**, 731–749.

Van der Gaast S. J., Mizota C. and Jansen (1986) Curved smectite in soils from volcanic ash in Kenya and Tanzania: a low angle X-ray powder diffraction study. *Clays Clay Miner.* **34**, 665–671.

Verdes G. (1990) Solubilité des hydroxydes d'aluminium entre 20 et 300 °C. Propriétés thermodynamiques des principales espèces naturelles du systèmes Al_2O_3–H_2O. Thèse de l'Université Paul-Sabatier.

Verdes G., Gout R. and Castet S. (1992) Thermodynamic properties of the aluminate ion and of bayerite, boehmite, diaspore and gibbsite. *Eur. J. Mineral.* **4**, 767–792.

Vidal O. and Dubacq B. (2009) Thermodynamic modelling of clay dehydration, stability and compositional evolution with temperature, pressure and H_2O activity. *Geochim. Cosmochim. Acta* **73**, 6544–6564.

White A. F. and Brantley S. L. (2003) The effect of time on the weathering of silicate minerals: why do weathering rates differ in the laboratory and field. *Chem. Geol.* **202**, 479–506.

Wielemaker W. G. and Wakatsuki T. (1984) Properties, weathering and classification of some soils formed in per-alkaline volcanic ash in Kenya. *Geoderma* **32**, 21–44.

Xu T., Apps J. A. and Pruess K. (2004) Numerical simulation of CO_2 disposal by mineral trapping in deep aquifers. *Appl. Geochem.* **19**, 917–936.

Zhou Z., Fyfe W. S., Tazaki K. and Van der Gaast S. J. (1992) The structural characteristics of palagonite from DSDP site 335. *Can. Mineral.* **30**, 75–81.

Associate editor: Jun-ichiro Ishibashi